Composite of methyl polysiloxane and avocado biochar as adsorbent for removal of ciprofloxacin from waters

Roberta A. Teixeira[1], Eder C. Lima[2,3,4], Antônio D. Benetti[1], Pascal S. Thue[3], Diana R. Lima[4], Farooq Sher[5], Glaydson S. dos Reis[6], Navid Rabiee[7,8], Moaaz K. Seliem[9], Mohamed Abatal[10]

[1-] *Graduate Program in Water Resources and Environmental Sanitation, Hydraulic Research Institute (IPH), Federal University of Rio Grande do Sul (UFRGS), Porto Alegre, RS, Brazil*

[2-] *Institute of Chemistry, Federal University of Rio Grande do Sul (UFRGS), Av. Bento Goncalves 9500, Porto Alegre, RS, Postal Box, 15003, ZIP 91501-970, Brazil*

[3-] *Graduate program in Science of Materials (PGCIMAT). Institute of Chemistry, Federal University of Rio Grande do Sul (UFRGS), Av. Bento Gonçalves 9500, Porto Alegre, RS, ZIP 91501-970, Brazil.*

[4-] *Graduate program in Mine, Metallurgical, and Materials Engineering (PPGE3M). School of Engineering, Federal University of Rio Grande do Sul (UFRGS), Av. Bento Gonçalves 9500, Porto Alegre, RS, Brazil*

[5-] *Department of Engineering, School of Science and Technology, Nottingham Trent University, Nottingham, NG11 8NS, United Kingdom*

[6-] *Department of Forest Biomaterials and Technology, Swedish University of Agricultural Sciences, Biomass Technology Centre, SE-901 83 Umeå, Sweeden*

[7-] *Department of Physics, Sharif University of Technology, P.O. Box 11155-9161, Tehran, Iran*

[8-] *School of Engineering, Macquarie University, Sydney, New South Wales, 2109, Australia*

[9-] *Faculty of Earth Science, Beni-Suef University, Beni-Suef, Egypt.*

[10-] *Facultad de Ingeniería, Universidad Autónoma del Carmen, Ciudad del Carmen C.P. 24153, Mexico*

* Corresponding author: profederlima@gmail.com or eder.lima@ufrgs.br

Abstract

Two carbon composite materials were prepared by mixing avocado biochar and methyl polysiloxane (MK). Firstly MK was dissolved in ethanol, and then the biochar was added at different times. In sample 1 (R1), the time of adding biochar was immediately after dissolving MK in ethanol, and in sample 2 (R_2), after 48 h of MK dissolved in ethanol. The samples were characterized by nitrogen adsorption/desorption measurements obtaining specific surface areas (S_{BET}) of 115 $m^2\ g^{-1}$ (R_1) and 580 $m^2\ g^{-1}$ (R_2). The adsorbents were further characterized using scanning electron microscopy, FTIR and Raman spectroscopy, adsorption of vapors of n-heptane and water, thermal analysis, Bohem titration, pHpzc, C H N elemental analysis. R_1 and R_2 adsorbents were employed as adsorbents to remove the antibiotic ciprofloxacin from the waters. The $t_{1/2}$ and $t_{0.95}$ based on the interpolation of Avrami-fractional-order were 20.52 and 246.4 min (R_1) and 14.00 and 157.6 min (R_2), respectively. Maximum adsorption capacities (Q_{max}) based on the Liu isotherm were 10.77 (R_1) and 63.80 mg g^{-1} (R_2) for ciprofloxacin. The thermodynamic studies showed a spontaneous and exothermic process for both samples, and the value of $\Delta H°$ is compatible with physical adsorption.

Keywords: methyl polysiloxane and biochar composite; hydrophobic surface; pharmaceutical adsorption; adsorption thermodynamics; synthetic effluents.

1 Introduction

Releases of contaminants of emerging concerns (CECs) to water bodies have been a critical environmental concern in the last years (Sophia and Lima, 2018) because these compounds can distress the aquatic ecosystem (Ma et al., 2022). These CECs come from the pesticides, pharmaceutical, textile, petrochemical industries, human and animal excretions, and hospital effluents (Sophia and Lima 2018). One pharmaceutical class of relevant concern to the environment is the antibiotic class, which humans and livestock frequently employ. The release of antibiotics into water bodies could generate microbial resistance (Qiu et al., 2019; Bondarczuk and Piotrowska-Seget, 2019); therefore, its removal from water is relevant.

The municipal wastewater treatment plants present failures in removing antibiotics and other CECs (Wang R et al., 2021) completely. Therefore, tertiary water treatment procedures are necessary to complete the removal of CECs (Arefi-Oskoui et al., 2022; Tian et al., 2022).

The methods for treatment of antibiotic contaminated waters take place using membrane filtration (Arefi-Oskoui et al., 2022), Fenton-like advanced oxidative process (Tian et al., 2022; Yu et al., 2022), photocatalysis (Baaloudj et al., 2021), ozone treatment (Foroughi et al., 2022), plasma degradation (Li et al., 2021), and adsorption (Arif et al., 2022; de Oliveira Carvalho et al., 2010; Guellati et al., 2022; Kovtun et al., 2020; Magesh et al., 2022).

Adsorption is preferable for antibiotic-loaded wastewater treatment due to its low-initial effectuation costs, easy operation, and high adsorption effectiveness of CECs from wastewaters (Caicedo et al., 2020; dos Reis et al., 2016; Thue et al., 2020; Tomul et al., 2020, Yazidi et al., 2020, Sellaoui et al., 2021).

The most commonly employed adsorbent utilized to remove pharmaceuticals from aqueous effluents is activated carbon (de Oliveira Carvalho et al., 2010; Thue et al., 2018; Hanafy et al., 2021, Sellaoui et al., 2017, 2019) and other carbon-based adsorbents such as biochar (Tomul et al., 2020). On the other hand, different composite materials (Arif et al., 2022; Caicedo et al., 2020; dos Reis et al., 2016; Guellati et al., 2022; Khan et al., 2020; Kovtun et al., 2020; Lawal et al., 2019; Magesh et al. 2022; Thue et al., 2020; Wang, Q et al., 2021;

Yadav et al., 2021; Yu et al., 2018, Sellaoui et al., 2022) are used as alternatives to activated carbons. In addition, adsorbents derived from polysiloxanes have been utilized to remove pharmaceuticals (dos Reis et al., 2016; Kollarahithlu and Balakrishnan, 2021; Panahi et al., 2019).

Polysiloxane composite materials have some benefits as adsorbents, such as high stability at a higher temperature, better mechanical strength, no swelling (dos Reis et al. 2016), and the facility of being chemically modified and functionalized because of the presence of free silanol groups on their surfaces (Çok and Gizli, 2020). On the other hand, polysiloxane's hybrid materials are more costly adsorbents than biochar and other biomass-based materials produced from low-cost biomass precursors (Cunha et al., 2020; Lima, DR et al., 2019a; Thue et al., 2017).

Avocado seed corresponds to approximately one-quarter of the total fruit (Leite et al., 2017). The annual production of Avocado in Brazil surpasses 240,000 tons, which will generate about 60,000 tons of avocado seed (STATISTA, 2020). In addition, the preparation of activated biochar from avocado seed as an adsorbent has been reported in the literature (Leite et al., 2017, 2018; Kudo et al., 2020); however, this material presents the drawbacks of low mechanical strength.

Therefore, combining avocado seed biochar and synthetic polysiloxane material precursors and producing a new composite material seems to be a clever strategy to use a biomass-based material and polysiloxane to obtain adsorbent with mechanical strength and good sorption capacity. Furthermore, this composite material should present rigidity and elevated hydrophilic behavior, and it could be used as adsorbents for a large number of CECs.

For the first time, the production of new composite adsorbent materials is reported using avocado biochar and methyl polysiloxane (MK) at a 1: 0.5 ratio. Firstly MK was dissolved in ethanol, and then the avocado biochar was added at different times. In sample 1 (R1), the time of adding biochar was immediately after dissolving MK in ethanol, and in sample 2 (R_2), after 48 h of MK dissolved in ethanol. Subsequently, different analytical techniques fully characterized the samples R_1 and R_2. The adsorbents R_1 and R_2 were used to remove

ciprofloxacin (CIP) from aqueous effluents.

This work chose ciprofloxacin (CIP) as the adsorbate because it is a broad-spectrum antibiotic largely employed for various treatments (Igwegbe et al., 2021; Sadredinamin et al., 2022). Also, it has been discovered that the toxicity of CIP present in aquatic phytoplankton and algae (Nie et al., 2013; Hagenbuch and Pinckney, 2012). Therefore the study of removing CIP antibiotic from aqueous effluents is indeed important.

2. Materials and Methods

2.1 Reactants and solutions

In order to prepare the composite material, methylpolysiloxane (MK) was provided by Silres® MK. Ciprofloxacin (CIP, $C_{17}H_{18}FN_3O_3$ MM: 331.347 g mol^{-1}, CAS: 86393-32-0, Fig S1) was furnished by Merck.

A 1.00 g L^{-1} stock solution of CIP was prepared using deionized water. The working CIP solutions were prepared by dilution of the stock solution.

2.2. Preparation of polysiloxane and biochar

The avocado biochar was prepared by carbonizing 50.0 g of avocado seed powder at 500°C using the conditions previously described (Leite et al., 2018).

Composite adsorbents prepared from avocado biochar and MK polysiloxane were prepared following the procedure. Briefly, 5.0 g MK was dissolved in 50.0 mL ethanol, and immediately after the dissolution of MK (about 15 min), 10.0 of avocado biochar was added and 0.5 mL NH_3. The system was kept under reflux at 70°C for 48 h. Afterward, the heating was stopped, the reactional mixture was filtered, and the product was washed with water + ethanol mixture (1:1). Finally, the product was dried at 130°C for 12 h. This first product was called (R_1). Then, a second procedure was carried out when the avocado

biochar was added after 48 h of dissolution of MK in water in the presence of NH_3 solution. In this case, the biochar was added after hydrolysis, and polycondensation of MK was already taken (R_2) before adding avocado biochar. The reactional mixture was stirred for 1 h, and then the reaction was stopped, and the final product was washed with ethanol + water (1:1) and dried at 130° for 12 h (R_2) (see Fig S2).

2.3. Composite characterizations

R_1 and R_2 composite adsorbents (< 250 µm) were used in the batch contact adsorption to decrease diffusion limitation when a larger particle diameter is employed.

Nitrogen adsorption/desorption isotherm analysis (Tristar 3000 apparatus, Micrometrics Instrument Corp.) was carried out to determine the surface area (BET method) (Thommes et al. 2015) and the volume of pores (by DFT method) (Jagiello and Thommes, 2004). Before the analysis, the sample was degassed at 100°C for 2 h in a nitrogen flow.

As previously described, the hydrophobic-hydrophilic ratio (HI) was performed (Teixeira et al., 2021; Wamba et al., 2017). In addition, the pH_{pzc} of the R_1 and R_2 samples were obtained as described elsewhere (Lima, DR et al., 2019b; Teixeira et al., 2021). The elemental analysis (C H N/O) was performed utilizing a Perkin Elmer analyzer (Lima, DR et al., 2019b; Teixeira et al., 2021).

The functional groups of the materials were qualitatively determined using Fourier Transform Infrared Spectroscopy (FTIR) (Bruker Spectrometer) using KBr pellets. The spectrum was recorded with 100 cumulative scans over 4000–400 cm^{-1} with a resolution of 4 cm^{-1} (Lima, DR et al. 2019b). In addition, Raman spectra were obtained using a Bruker Bravo spectrometer (Guy et al., 2022).

An adapted Boehm-titration procedure was used to quantify the total amount of acidic and basic groups of the ABc-600 (Goertzen et al., 2010; Oickle et al., 2010).

The thermal stability of the R_1 and R_2 were performed by TGA analysis (TA model SDT Q600) as previously described (Lima, DR et al., 2019b; Thue et al., 2020).

The morphology of composite samples to observe the particle patterns was examined by Scanning Electron Microscopy (SEM) using the Merlin instrument (FESEM, ZEISS Sigma HD) with an in-lens secondary electron detector (dos Reis et al., 2022).

2.4 Batch adsorption experiments

An aliquot of 20.00 mL of CIP (see Fig S1) solution with the initial concentration variating from 5.0 to 200.0 mg L^{-1} was added to 50.0 mL flat-Falcon tubes with 30.0 mg of R_1 and R_2 composite samples at pH ranging 2.0-10.0. The Falcon tubes were capped and disposed of horizontally inside a thermostatic reciprocating agitator (Oxy 350, São Leopoldo, Brazil). The slurries were shaken at different time intervals between 1 and 360 min at 10° to 45°C with a shaking speed of 120 strikes per minute (Teixeira et al., 2021). Subsequently, the solid phase was separated from the liquid phase by centrifugation. When necessary, aliquots of 1-10 ml of the liquid phase were diluted to 1.0-25.0 mL in calibrated volumetric flasks using the blank solution. Ciprofloxacin unadsorbed after the adsorption process was measured using the T90+ PG Instruments spectrophotometer at a maximum absorption wavelength of 273.0 nm (de Oliveira et al., 2019).

The sorption capacity (Eq 1) and the percentage of CIP removed (Eq 2) are given below:

$$q = \frac{(C_0 - C_f)}{m}.V \quad (1)$$

$$\%\ Removal = 100.\frac{(C_0 - C_f)}{C_0} \quad (2)$$

q is the sorption capacity of CIP adsorbed by the adsorbent (mg g^{-1}). C_o is the initial CIP solution concentration in contact with the solid adsorbent (mg L^{-1}). C_f is the final CIP concentration after adsorption (mg L^{-1}). m is the mass of adsorbent (g). V is the aliquot of the

pharmaceutical solution (L) introduced in the flask.

The study of the influence of the initial pH of CIP was performed at 25°C, using an initial concentration of 100 mg L^{-1} of the pharmaceutical solution, a time of contact between the adsorbent and adsorbates of 2 h, an adsorbent dosage of 1.5 g L^{-1}, and pH ranging from 2.0 to 10.0.

The kinetic and equilibrium data's fitness was done using nonlinear methods, which were evaluated using the Simplex method and the Levenberg–Marquardt algorithm using the fitting facilities of the Microcal Origin 2021 software (Lima et al., 2021a). The suitableness of the kinetic and equilibrium models was evaluated using the residual sum of squares (*RSS*), the determination coefficient (R^2), the adjusted determination coefficient (R^2_{adj}), the standard deviation of residues (*SD*), and also the Bayesian Information Criterion (*BIC*) (Lima et al., 2021a, 2021b). Equations 3 to 7 are the mathematical expressions for respective *RSS*, R^2, R^2_{adj}, *SD, and BIC*.

$$RSS = \sum_{i}^{n} \left(q_{i,exp} - q_{i,model}\right)^2 \quad (3)$$

$$R^2 = \left(\frac{\sum_i^n \left(q_{i,exp} - \overline{q}_{i,exp}\right)^2 - \sum_i^n \left(q_{i,exp} - q_{i,model}\right)^2}{\sum_i^n \left(q_{i,exp} - \overline{q}_{i,exp}\right)^2} \right) \quad (4)$$

$$R^2_{adj} = 1 - (1 - R^2).\left(\frac{n-1}{n-p-1}\right) \quad (5)$$

$$SD = \sqrt{\left(\frac{1}{n-p}\right).\sum_{i}^{n} \left(q_{i,exp} - q_{i,model}\right)^2} \quad (6)$$

$$BIC = nLn\left(\frac{RSS}{n}\right) + pLn(n) \quad (7)$$

In the above equations, $q_{i,\ model}$ is the individual theoretical q value predicted by the model; $q_{i,\ exp}$ is individual experimental q value; $\overline{q}_{exp}$ is the average of all experimental q values measured; n is the number of experiments; p is the number of parameters in the fitting model.

The values of R^2adj, SD, and BIC will be presented to compare different models of kinetics and equilibrium presented in this work. The best-fitted model would present R^2_{adj} closer to 1.000, lower values of SD, and BIC values. However, the kinetic and equilibrium model could not merely be chosen based on the values of R^2 (Lima et al., 2021a, 2021b) when these models present a different number of parameters. Therefore, it is necessary to check if the R^2 values' improvements are due to the increase of a number of the parameters (Lima et al., 2021a, 2021b) or if, physically, the model with more parameters explains better the process taking place (Lima et al., 2021a, 2021b).

However, the difference in BIC values between models could be conclusive if the difference in BIC values ≤ 2.0, there is no significant difference between the two models (Lima et al., 2021a, 2021b). When BIC values' difference is within 2-6, there is a positive perspective that the model with lower BIC is the most suitable (Lima et al., 2021a, 2021b). For variations of BIC values from 6-10, there is a strong possibility that the model with a lower BIC value is the best model to be fitted [43,44]. However, if the difference in BIC values ≥ 10.0, it can be predicted with accuracy that the model with a lower BIC value is better fitted (Lima et al., 2021a, 2021b).

2.5. Kinetics and equilibrium adsorption models

Pseudo-first-order, pseudo-second-order, and Avrami fractional-order (Lima et al., 2021a) models were used to fit the kinetic data. The mathematical equations of these respective models are shown in Equations 8, 9, and 10.

$$q_t = q_e.[1\text{-}exp(\text{-}k_1 t)] \quad (8)$$

$$q_t = \frac{k_2.q_e^2.t}{1 + q_e.k_2.t} \quad (9)$$

$$q_t = q_e.[1 - exp\,(-k_{AV}.t)^{nAV}] \quad (10)$$

Where t is the contact time (min); q_t, q_e are the amount of adsorbate adsorbed at time t and the

equilibrium, respectively (mg g^{-1}); k_1 is the pseudo-first-order rate constant (min^{-1}); k_2 is the pseudo-second-order rate constant (g mg^{-1} min^{-1}); k_{AV} is the Avrami-fractional-order constant rate (min^{-1}), n_{AV} is the Avrami exponent (n >0).

Langmuir, Freundlich, and Liu's models were employed to analyze equilibrium data. Equations 11, 12, and 13 show the corresponding Langmuir, Freundlich, and Liu models (Lima et al., 2021a).

$$q_e = \frac{Q_{max}.K_L.C_e}{1 + K_L.C_e} \quad (11)$$

$$q_e = K_F.C_e^{1/nF} \quad (12)$$

$$q_e = \frac{Q_{max}.(K_g.C_e)^{nL}}{1 + (K_g.C_e)^{nL}} \quad (13)$$

Where q_e is the adsorbate amount adsorbed at equilibrium (mg g^{-1}); C_e is the adsorbate concentration at equilibrium (mg L^{-1}); Q_{max} is the maximum sorption capacity of the adsorbent (mg g^{-1}); K_L is the Langmuir equilibrium constant (L mg^{-1}); K_F is the Freundlich equilibrium constant [$mg.g^{-1}.(mg.L^{-1})^{-1/nF}$]; K_g is the Liu equilibrium constant (L mg^{-1}); n_F and n_L are the exponents of Freundlich and Liu model, respectively, (n_F and n_L are dimensionless).

2.6 Adsorption thermodynamics

Thermodynamic studies for the CIP adsorption onto R_1 and R_2 adsorbents were performed at temperatures ranging from 10ºC to 45°C (283 to 318K).

The Gibb's free energy change (ΔG^0, kJ mol^{-1}), enthalpy change ($\Delta H°$, kJ mol^{-1}), and entropy change (ΔS^0, J $mol^{-1}K^{-1}$) were evaluated with the aid of Equations 14-17, respectively (Lima, EC et al., 2019a, 2019b, 2020).

$$\Delta G^0 = \Delta H^0 - T.\Delta S^0 \quad (14)$$

$$\Delta G^0 = -RT.LnK_e^0 \quad (15)$$

$$K_e^0 = \frac{(1000.K_g.Mw.[adsorbate]^0}{\gamma} \quad (16)$$

The combination of Equations 14 and 15 leads to equation 17

$$LnK_e^0 = \frac{\Delta S^0}{R} - \frac{\Delta H^0}{R}.\frac{1}{T} \quad (17)$$

248

249 R is the universal gas constant (8.314 J K^{-1} mol^{-1}); T is the absolute temperature
250 (Kelvin); M_w is the molecular weight of the adsorbate (g mol^{-1}), $[adsorbate]^0$ is the standard
251 molar concentration of the adsorbate, which by definition is 1 mol L^{-1}; γ is the activity coefficient
252 of the adsorbate. K_e^0 is the thermodynamic equilibrium constant, calculated according to
253 equation 16. K_e^0 is dimensionless (Lima, EC et al., 2019a, 2019b).

254 K_e^0 is calculated by converting K_g values (Liu equilibrium constant) or K_L (Langmuir
255 equilibrium constant), expressed in L mg^{-1} into L mol^{-1}. Firstly, the value K_g or K_L is multiplied
256 by 1000 (mg g^{-1}), and then multiplied by the molecular weight of the adsorbate (g mol^{-1}) and
257 by the standard concentration of the adsorbate (1 mol L^{-1}) and divided by the activity coefficient
258 of the adsorbate (γ- dimensionless) (Lima, EC et al., 2019a, 2019b). It is assumed that the
259 solution is sufficiently diluted to consider that the γ is unitary (Lima, EC et al., 2019a, 2019b).
260 Making these calculations, K_e^0 becomes dimensionless (Lima, EC et al., 2019a, 2019b).

261 Equation 17 is the linearized van't Hoff equation (Lima, EC et al., 2020). On the other
262 hand, recently, Lima et al. 2020 proposed using the nonlinear van't Hoff equation, as presented
263 in equation 18.

$$K_e^\Theta = exp\left[\frac{\Delta S^\Theta}{R} - \left(\frac{\Delta H^\Theta}{R}\right).\frac{1}{T}\right] \quad (18)$$

264

265

266 **3. Results and discussion**

267

268

269 *3.1. Textural characteristics*

270

Fig 1 shows the isotherms of adsorption and desorption of N_2 and the pore size distribution curves according to the DFT method for R_1 and R_2 composite samples.

Insert Fig 1

There is a remarkable difference in the textural properties of composite materials. R_1 sample presents a surface area of 115 m^2 g^{-1} and a total pore volume of 0.0713 cm^3g^{-1}. Conversely, the R_2 sample presents a surface area of 580 m^2 g^{-1} and a total pore volume of 0.364 cm^3 g^{-1}. It is crucial to focus that although the adsorption isotherm of adsorption of N_2 seems to be classified as type I (Thommes et al., 2015), they present hysteresis type H2(b) (Thommes et al., 2015). This type of loop hysteresis is associated with a wide size distribution of neck widths of the pores (Thommes et al., 2015). The ratio P/P_0 to about 0.2 is assigned to a monolayer of nitrogen formation over both composite adsorbents (Thommes et al., 2015).

The pore size distribution curves of the materials seem to be a mixture of microporous materials (pore diameter < 2 nm) and mesopores with diameter < 8 nm (Fig 1B and 1D).

It is expected that R_2 composite material would present a higher sorption capacity for removal of CIP from waters than R_1 due to the higher surface area and total pore volume (dos Reis et al., 2016; Thue et al., 2020). This enhancement of the expected sorption capacity of R_2 material over R_1 is due to the pore-filling mechanism. Although this mechanism is essential for removing solutes dissolved in water, it is not the unique mechanism that should be considered (Cunha et al., 2020; Thue et al., 2017).

Fig S3 shows the SEM images of R_1 and R_2 composite samples, respectively. There are no remarkable differences between the two composite materials. In the R_1 sample, an irregular material deposit is seen over other materials. This deposit could be chains of MK polysiloxane covering the avocado biochar. In the R_2 composite sample, the layer of MK polysiloxane seems to be shorter than the one covering R_1. The results of EDS (data not shown) did not reveal remarkable differences in the Si content in both samples; however, further analysis will show that the R_1 material presents more Si content when compared to the R_2 sample.

3.2 Qualitative analysis

With the aim of identifying the main functional groups present on the surface of the R_1 and R_2 composite materials, FTIR spectra were recorded, contributing to a better understanding of how the composite materials could interact with the CIP adsorbate (see Fig 2).

Insert Fig. 2

Both composite materials present very similar FTIR spectra. The band at 3417 (R_1) and 3415 cm^{-1} (R_2) corresponds to the stretching of the -OH group (de Oliveira Carvalho et al., 2010; Caicedo et al., 2020). Considering that these bands are broad, they should be overlapping with -NH groups. For R1, the bands at 2968 (asymmetric), 2922 (asymmetric), and 2854 cm^{-1} (symmetric) could be assigned to the stretch of C-H groups (Thue et al., 2017; Wamba et al., 2017), and for R_2, the bands at 2976 (asymmetric), 2920 (asymmetric), and 2856 cm^{-1} (symmetric) are C-H stretching (Thue et al., 2017; Wamba et al., 2017). The bands at 1691 (R_1) and 1689 cm^{-1} (R_2) are assigned to the stretching of the C=O carboxylic acid functional group in biochar (Guy et al., 2022; Teixeira et al., 2021). The bands at 1621 and 1570 (R_1) and 1614 and 1566 cm^{-1} (R_2) are attributed to aromatic rings mode (dos Reis et al., 2022; Tomul et al., 2020). A broadening of these bands was observed, that is, characteristics of organo-silicate materials (dos Reis et al., 2016; Teixeira et al., 2021). In addition, the bands at 1570 (R_1) and 1566 cm^{-1} (R_2) can also be attributed to the overlap of NH_2 bending bands with aromatic ring modes (dos Reis et al., 2016; Teixeira et al., 2021). The small bands at 1406 (R_1) and 1408 (R_2) are attributed to aromatic ring modes (Thue et al., 2017; Wamba et al., 2017). The bands at 1269 (R_1) and 1271 cm^{-1} (R_2) are assigned to the C-O stretching of the phenolic group present on the biochar (Lima, DR et al. 2019a; b) or alternatively to Si-CH_3 of MK present in both samples (dos Reis et al., 2016; Teixeira et al., 2021). The bands at 1110 (R_1), and 1120 cm^{-1} (R_2) are assigned to C-O of secondary alcohols present in the biochar. Both composite materials present a band at 1026 (R_1), and 1032 cm^{-1} (R_2) attributed to the Si-O-Si stretch of composite material (dos Reis et al., 2016; Teixeira et al., 2021) or primary alcohol C-O groups stretch (Cunha et al. 2020; Thue et al. 2017). The band at 766 (R1) and 769 cm^{-1} (R_2) are attributed to Si-O stretching (Çok and Gizli, 2020; Thue et al., 2017).

The Raman spectra of R_1 and R_2 composites are depicted in Fig 3.

Insert Fig 3.

Raman spectroscopy was carried out to deeply explore the structure and degree of graphitization of the R_1 and R_2 composite materials. Two distinct Raman shifts are observed in the spectra. The first one (D-band), centered at 1332 cm^{-1}, is assigned to sp^3 electronic states (considered defects in the planar sp^2 graphitic structure) corresponding to graphite's low symmetry carbon structure (dos Reis et al., 2022). The second band (G-band), centered at 1592 cm^{-1}, reflects the structural integrity of sp^2-hybridized carbon atoms (dos Reis et al., 2022). These two types of carbon are present in the BCs phase.

The qualities of the samples were evaluated by comparing the D to G band intensity (the ID/IG ratio). The ID/IG ratio is often below a couple of percent for high-quality samples with higher graphitization. Therefore, higher ID/IG ratio values mean carbon structure with several defects, and low values mean carbon samples with a higher organization (dos Reis et al., 2022). The value of ID/IG for R_1 was 1.04, and for R_2, it was 0.800. These results show that the grafting of MK polysiloxane onto avocado biochar led to a more organized R_2 composite sample when less MK is grafted in the biochar (data will be shown in the next section that R_2 presents less Si than the R_1 sample).

3.3 Quantitative analysis

The thermal gravimetric analyses of R_1 and R_2 composite samples are shown in Fig 4. The thermal behavior of both composite samples is similar, presenting three main weight losses. This analysis utilized nitrogen from room temperature up to 800°C and then from 800° to 1000°C; the atmosphere was changed from inert to oxidizing utilizing synthetic air (Cunha et al., 2020; Lima, DR et al., 2019a; b; Teixeira et al., 2021; Thue et al., 2020).

In the first stage, 21.3°-530.2°C (R_1) and 18.3°-522.2°C (R_2) comprise the water losses associated with some small decomposition of volatile organics present in the avocado biochar (Cunha et al., 2020; Leite et al., 2018; Lima, DR et al., 2019b; Teixeira et al., 2021) or the loss of methyl group present in the MK siloxane (dos Reis et al., 2016). However, these weight

losses were only 7.51% (R_1) and 6.04% (R_2), showing the high-thermal stability of both composite samples. The second stage was 530.2°-796.6°C (R_1) and 522.2°-807.0°C (R_2), which could be assigned to some degradation of carbon material of biochar. Again, this weight loss was not remarkable for both samples (8.85% R_1 and 6.50% R_2), which indicates that from room temperature up to close to 800°C, the total weight loss under nitrogen stream was 16.36% (R_1) and 12.54% (R_2). These values indicate that both composite materials present very high thermal stability.

In the third stage, under a synthetic air atmosphere, the weight losses were remarkably increased to 53.37% (R_1) and 60.83% (R_2). This third weight loss corresponds to the total degradation of the composite materials' carbonaceous matrix, leading to a total weight loss including the three stages up to 69.73% (R_1) and 73.37 (R_2). Therefore, the residual mass left in the crucible was 30.27% (R_1), and 26.63% (R_2) could be assigned to the ashes of the composite samples since the third stage was conducted under a synthetic air atmosphere (Cunha et al., 2020; Lima, DR et al., 2019a; b; Teixeira et al., 2021; Thue et al., 2020).

Insert Fig 4

Based on these residue's contents, it is possible to infer that the contents of MK incorporated in R_1 were higher than in the R_2 sample. This result is consistent with the time of exposition of avocado biochar with MK polysiloxane. In the R_1 sample, the avocado biochar was added immediately after the dissolution of MK in ethanol, and they remained together for 48 h of contact. On the other hand, for the R_2 sample, the avocado biochar was added after 48 h of dissolution of MK polysiloxane in ethanol, allowing to form oligomers of MK in ethanol, adding the avocado biochar, and keeping it together for just one hour of contact.

The C H N elemental analysis is depicted in Table 1. The contents of carbon present in R_1 are compatible with a higher composite formation between avocado biochar and MK polysiloxane because then its value is lower (53.64% C) when compared with the R_2 sample (61.22% C), and also the value is also compatible with the contents of ashes determined by TGA analysis, described previously. The contents of H and N were also determined by CHN

elemental analysis, and the values are depicted in Table 1. The atomic ratio C/H is 1.20 (R_1) and 1.71 (R_2). How much the C/H atomic ratio is closer to 2, the higher the degree of aromaticity. Conversely, when the atomic ratio of C/H is closer to 1, higher is the aliphatic portion (dos Reis et al., 2022).

This behavior could be easily explained by imaging the condensation of several aromatic rings. For each aromatic ring (C_6H_6), when they are fused, it is necessary to lose two atoms of hydrogen, forming $C_{10}H_8$ for two rings, $C_{14}H_{10}$ for three fused aromatic rings, $C_{18}H_{22}$ for four fused aromatic rings, $C_{22}H_{14}$ for five fused rings, $C_{26}H_{16}$ for six fused aromatic rings. Therefore, for each fusion of two aromatic rings, the number of carbon increases by four, and the number of hydrogen increases by two (ratio of 2C for 1H).

Considering that the methyl group number of MK polysiloxane is higher when more of this MK is grafted on the biochar. Therefore, the values of C H N elemental analysis are compatible with a higher amount of MK grafted on R_1 when compared with the R_2 sample.

The total acidity and basicity of the composite samples were quantified using the Bohem titration (Goertzen et al. 2010; Oickle et al. 2010), and the contents of these groups are depicted in Table 1. The higher the sum of acidic plus basic groups, the more polar the surface of the adsorbent.

The HI ratio is given by the equation below (dos Reis et al., 2016; Cunha et al., 2020):

$$HI = \frac{amount\ of\ n-heptane\ vapor\ (mg) \Big/ adsorbent\ mass\ (g)}{amount\ of\ water\ vapor\ (mg) \Big/ adsorbent\ mass\ (g)} \quad (1)$$

The HI values of R_1 and R_2 samples are also depicted in Table 1. The values of HI were 1.725 (R_1) and 1.051 (R_2). According to Equation 1 given above, higher values of HI means a higher tendency of the adsorbent surface to uptake hydrophobic molecules. As discussed previously, the sum of acidic plus basic groups was 0.2081 mmol g^{-1} (R_1) and 0.5742 (R_2). Comparing the values of HI with the sum of polar groups (acidic plus basic groups), it can be observed that a higher amount of polar groups leads to a low value of HI, as previously

observed in several cases already reported in the literature (Cunha et al. 2020; dos Reis et al. 2016; Lima et al. 2019a; b; Leite et al. 2017; Teixeira et al. 2021; Thue et al. 2020). Another important correlation is that the higher the amount of MK incorporated, the higher the hydrophobicity and HI value. Considering that the R_1 sample presented a higher amount of MK grafted on the biochar, this material presents a higher HI value.

The values of pH_{pzc} of R_1 and R_2 were 5.09 and 4.91, respectively (Table 1), showing no remarkable difference in the acidity behavior of these two composite materials.

Insert Table 1.

3.4 Effect of pH

The influence of the adsorbate solution's initial pH on the sorption capacity is one of the main variables that could affect the uptake of a molecule in an adsorbent (Kudo et al., 2020; Tomul et al., 2020).

The value of pH_{pzc} also influences the sorption capacity of the adsorbent. For pH values > pH_{pzc}, the adsorbent surface becomes negatively charged, and for pH values < pHpzc, the adsorbent surface becomes positively charged (Leite et al., 2017; Lima, DR et al., 2019a). Also, the pKa values of the adsorbate influence the sorption capacity of an adsorbent. Fig.S4 shows the CIP species at pH ranging from 0 to 14 (de Oliveira Carvalho et al., 2019). The pKa values of CIP are pK_{a1} 5.56 and pK_{a2} 8.77. Therefore, CIP has three species with different proportions depending on the pH value (see Fig S4). At pH 7.0, species 1 contributes 3.48%, species 2 contributes 94.84%, and species 3 contributes 1.63% of all the species (de Oliveira Carvalho et al., 2019). Then, the zwitterionic species is predominant at pH 7 (species 2, see Fig. S4). Assays of the effect of initial CIP pH ranging from 3.5 to 12 demonstrated that the removal percentage of CIP did not suffer a remarkable variation (changes < 2.3%). Then, in the next adsorption experiments, the pH of the adsorbate solution was fixed at 7.0 to continue this research.

It is important to highlight that at pH 7.0, the surface of R_1 and R_2 samples will be negatively charged; however, the predominant species of CIP is a zwitterionic species (94.84%) (de Oliveira Carvalho et al., 2019); therefore, electrostatic attraction of the quaternary ammonium salt with the negatively charged adsorbent could take place.

3.5. Kinetic studies.

The kinetics adsorption data of the CIP antibiotic onto R_1 and R_2 composite samples were carried out utilizing the pseudo-first-order, pseudo-second-order, and Avrami-fractional-order (Lima et al., 2021a; b), and the parameters of the fitted models are shown in Table 2, and the kinetic curves are shown in Fig 5.

Insert Fig 5.

Insert Table 2

Observing Fig 5, it is possible to verify that PFO and PSO kinetic adsorption models were not accurately fitted since most experimental points are out of the model curve. On the other hand, a sound analysis of Table 2 clarifies it. The values of R^2_{adj}, SD, and BIC show that the Avrami-fractional-order kinetic adsorption model was the unique model that described the kinetic adsorption data well because the values of R^2_{adj} are closer to 1.00, the values of SD and BIC were lower than compared with PFO and PSO. As reported earlier (Lima et al. 2021a; b), the Bayesian Information Criterion (BIC) is a Statistical Analysis that establishes the best-fitted model because when ΔBIC (BIC model 1 – BIC model 2) < 2, there is no remarkable difference between the two models, and when ΔBIC > 10, certainly the model with lower BIC value is the model that better describes the physical phenomenon (Lima et al. 2021a; b). The ΔBIC between PFO and Avrami and PSO and Avrami were respectively 156.7 and 134.5 for R_1 adsorbent and 65.09 and 28.52 for R_2 adsorbent. Therefore, the Statistical Analysis confirms that the Avrami-fractional kinetic model describes the adsorption kinetics for CIP uptake using R_1 and R_2 adsorbents.

Considering that it is not easy to compare different kinetic models because the constant rates present different units (see Table 2), the values of $t_{1/2}$ and $t_{0.95}$ were obtained by interpolation in the fitted curve for the time necessary to attain 50% and 95% of the saturation, respectively (Lima, DR et al., 2019b; Teixeira et al., 2021; Wamba et al., 2017). These time parameters mean the time necessary to attain 50% and 95% of the saturation, respectively. Considering that the Avrami fractional-order kinetic model was the best-fitted model, it can be assumed that the times to attain 95% of saturation were 246.4 min (R_1) and 157.6 min (R_2). Based on this result, it was established that the equilibrium studies should employ a contact time between the adsorbent and the adsorbate of 300 min (R_1) and 180 min (R_2) for performing these experiments.

This difference in the contact time to attain the equilibrium is coherent with the total pore volume of R_1 (0.0713 cm^3g^{-1}) and R_2 (0.364 cm^3 g^{-1}) composite materials, as earlier reported for other adsorbents (Cunha et al., 2020; Lima, DR et al., 2019a). Therefore, higher total pore volume will lead to faster kinetics (Cunha et al., 2020; Lima, DR et al., 2019a).

3.6 Equilibrium and thermodynamic studies and adsorption mechanism

The equilibrium adsorption studies of CIP onto R1 and R2 composite samples were performed from 10° to 45°C. The Langmuir, Freundlich, and Liu equilibrium models accessed CIP uptake. The results are depicted in Fig 6 (R_1) and Fig 7 (R_2), and the values of equilibrium parameters are shown in Table 3.

Insert Fig 6

Insert Fig 7

Insert Table 3.

Results depicted in Table 3 show that the Liu equilibrium model was the best equilibrium model for all the studied temperatures (10° to 45°C) due to R^2_{adj} being closer to 1 and the lowest BIC and SD values. The ΔBIC between Langmuir and Liu ranged from 50.00 to 220.4

(10°- 45°C) using R_1 adsorbent and 72.46 to 206.9 (10° - 45°C) using R_2 adsorbent (Lima et al., 2021a; b). The ΔBIC between Freundlich and Liu ranged from 69.18 to 141.8 for R_1 adsorbent and ranged from 107.3 to 241.1 for R_2 adsorbent. Therefore, ΔBIC values were much higher than 10, which allows one to state that the Liu isotherm model was the equilibrium model that could explain the equilibrium data for CIP adsorption onto R_1 and R_2 composite samples at the temperature of 10°- 45°C. These results are corroborated with the values of R^2_{adj} closer to 1.00, besides the lowest values of SD (see Table 3).

Taking into account the values of Q_{max} obtained by the Liu isotherm model for R_1 and R_2 samples, it is observed that R_2 presented Q_{max} values 5.92-6.50 times higher than R_1. This remarkable difference is compatible with the differences in the surface area (580 $m^2\ g^{-1}$ for R_2 versus 115 $m^2\ g^{-1}$ for R_1) and total pore volume (0.364 $cm^3\ g^{-1}$ for R_2 versus 0.0713 $cm^3\ g^{-1}$ for R_1). In this sense, pore-filling is one of the main mechanisms of adsorption.

The sorption capacity of R_1 and R_2 were compared with several other adsorbents, as depicted in Table 4 (Arif et al., 2022; Caicedo et al., 2020; de Oliveira et al., 2019; Guellati et al., 2022; Han et al., 2022; Karoui et al., 2020; Khan et al., 2020; Kovtun et al., 2020; Lam et al., 2021; Lawal et al., 2019; Magesh et al., 2022; Najafpoor et al. 2019; Rahman et al. 2021; Wang et al. 2020; Wang, Q et al. 2021; Wu et al., 2018; Wu et al., 2021; Xikhongelo et al., 2021; Yadav et al., 2021; Yang et al., 2020; Yu et al., 2018).

Insert Table 4.

Out of twenty-three adsorbents, the R_2 composite adsorbent presents a higher sorption capacity of nine (Arif et al., 2022; Caicedo et al., 2020; de Oliveira et al., 2019; Guellati et al., 2022; Han et al., 2022; Karoui et al., 2020; Khan et al., 2020; Kovtun et al., 2020; Lam et al., 2021; Lawal et al., 2019; Magesh et al., 2022; Najafpoor et al., 2019; Rahman et al., 2021; Wang et al., 2020; Wang, Q et al., 2021; Wu et al., 2018; 2021; Xikhongelo et al., 2021; Yadav et al., 2021; Yang et al., 2020; Yu et al., 2018). The sorption capacity of R_2 material is not remarkable compared to the literature, but it opens possibilities of being improved when other polysiloxanes are employed instead of MK.

Table 5 shows the thermodynamic parameters obtained from the equilibrium data from 10° to 45°C (283-318 K) using the best-fitted isotherm (Lima, EC et al., 2019a; b) for the uptake of CIP using R_1 and R_2 composite adsorbents. In addition, the nonlinear van't Hoff equation (Lima et al., 2020) is presented in Fig 8 as depicted in Table 5; all values of ΔG^{Θ} were negative, indicating that the adsorption process was favorable at the 283-318 K interval.

Insert Table 5

Insert Fig 8

Observing Fig 8, the enthalpy variation was negative (exothermic process) for CIP uptake on both composite samples, and the variation of entropy was also negative. These results show that CIP after the adsorption should be in a more organized state than free in the aqueous solution before the adsorption takes place (Lima et al., 2021a). Also, considering the magnitude of enthalpy, the values obtained for both adsorbents are compatible with a physical interaction of the CIP with R_1 and R_2 composite samples (Leite et al., 2017; 2018; Lima et al., 2021a). The adsorption process is controlled by enthalpy because the process is exothermic, which contributes to ΔG^{Θ} being negative in all the temperature range (283-318 K).

Based on the results of the characterization of the R_1 and R_2 adsorbents; the adsorption studies (adsorption kinetics, equilibrium, and thermodynamics), it is possible to establish a mechanism of adsorption that is depicted in Fig 9.

Insert Fig 9

CIP at pH 7.0 is present in the zwitterionic form (see Fig S4). When this antibiotic is placed with the composite materials R_1 or R_2, the cationic ammonium group of CIP has an acid-base interaction with donor groups present on the biochar part of the composite material (Tomul et al., 2020). In addition, the anionic group of CIP interacts with OH groups present on the biochar, forming hydrogen bonding (Leite et al., 2017; Tomul et al., 2020). Also, CIP presents a fluoride group that could form halogen bonding with the biochar or with the silane group on

R_1 and R_2 (Desiraju et al., 2013). CIP also could for π-π interactions with the aromatic rings present on the biochar part of the composite samples (Leite et al., 2017; Tomul et al., 2020). Besides the polar interactions, CIP could also interact with hydrophobic interactions (van der Waals forces) with the silane group present on the composite samples (Teixeira et al., 2021; Tomul et al., 2020; Wamba et al., 2017). As a result, the silane groups increase the R_1 composite sample's hydrophobicity compared with the R_2 composite sample.

On the other hand, higher coverage of the biochar with silane groups would impair the polar interactions of CIP with the polar groups present on the biochar. Therefore, this statement is justified that the R_1 composite sample presents more Si contents than the R_2 sample (see Fig 4). Moreover, a pore-filling mechanism explains the CIP uptake by the composite samples, being the composite material with higher surface area and higher total pore volume (R_2) the sample that presented higher sorption capacity to CIP antibiotic.

Conclusion

Two composite materials were prepared by mixing MK polysiloxane with avocado biochar. The synthesis route of both materials is practically the same, only changing the time for the addition of the avocado biochar to the dissolved MK solution in ethanol. The first composite material (R_1), the addition of avocado biochar, was immediately after dissolving the MK in ethanol at reflux. The second composite material (R_2), the addition of avocado biochar, was after 48 h dissolution of MK polysiloxane in ethanol, ane continuing the reflux for 1 h. The characterization of the R_1 and R_2 composite samples was carried out by isotherms of adsorption and desorption of nitrogen, which show that the surface area and total pore volume of R_2 were more than 5 times higher than R_1.

Furthermore, results of TGA analysis revealed that the amount of Si contents present on R_1 was higher than R_2, which provoked a higher hydrophobicity of R_1 (HI 1.725) than R_2 (1.051). In addition, the R_2 composite presented a higher number of functional groups (acidic plus basic groups) than R_1. The kinetic experiments of adsorption show that the CIP uptake

was faster in R_2 ($t_{1/2}$ 14.00, $t_{0.95}$ 157.6 min) when compared to R_1 composite sample ($t_{1/2}$ 20.52, $t_{0.95}$ 264.4 min). This faster kinetics is due to the higher pore volume of R_2 material. The equilibrium studies of R_1 and R_2 composite samples were obtained from 10°- 45°C (283-318 K) using three isotherm models. The best-fitted equilibrium results were obtained using the Liu isotherm model. The thermodynamic studies indicated that the adsorption process was favorable, spontaneous, and exothermic, and the magnitude of enthalpy changes was consistent with physical adsorption.

Author's contribution: Roberta A. Teixeira- investigation, Eder C. Lima- writing original draft, Antônio D. Benetti- supervising, Pascal S. Thue-conceptualization, Diana R. Lima- investigation, Farooq Sher- Visualization, Glaydson S. dos Reis- reviewing and editing, Navid Rabiee- reviewing and editing, Moaaz K. Seliem-- reviewing and editing, Mohamed Abatal- reviewing and editing.

Funding. CAPES, CNPq and FAPERGS

Acknowledgments

The authors are grateful to the Nanoscience and Nanotechnology Center (CNANO-UFRGS) of the Federal University of Rio Grande do Sul (UFRGS). We are also grateful to ChemAxon for giving us an academic research license for the Marvin Sketch software, Version 22.11.0 (http://www.chemaxon.com), 2022, used for molecule physical-chemical properties.

Data availability- Not applicable

Compliance with ethical standards

Competing interests- The authors declare no conflict of interest.

Ethical approval- Not applicable

Consent to participate- The manuscript is an original work of all authors, and all authors made a significant contribution to this study.

Consent to publish- The authors hereby consent to the publication of the work in the Environmental Science and Pollution Research journal.

References

References

Arefi-Oskoui S, Khataee A, Behrouz SJ, Vatanpour V, Gharamaleki SH, Orooji Y, Safarpour M (2022) Development of MoS_2/O-MWCNTs/PES blended membrane for efficient removal of dyes, antibiotics, and protein. Sep Purif Technol 280:1–14 10.1016/j.seppur.2021.119822

Arif M, Liu G, Zia ur Rehman M, Yousaf B, Ahmed R, Mian MM, Ashraf A, Munir MAM, Rashid MS, Naeem A (2022) Carbon dioxide activated biochar-clay mineral composite efficiently removes ciprofloxacin from contaminated water - Reveals an incubation study. J Clean Prod 332:1–14 10.1016/j.jclepro.2021.130079

Baaloudj O, Assadi I, Nasrallah N, El-Jery A, Khezami L, Assadi AA (2021) Simultaneous removal of antibiotics and inactivation of antibiotic-resistant bacteria by photocatalysis: A review. Journal of Water Process Engineering 42:1–11 10.1016/j.jwpe.2021.102089

Bondarczuk K, Piotrowska-Seget Z (2019) Microbial diversity and antibiotic resistance in a final effluent-receiving lake. Sci. Total Environ 650:2951–2961 10.1016/j.scitotenv.2018.10.050

Caicedo DF, dos Reis GS, Lima EC, de Brum IAS, Thue PS, Cazacliu BG, Lima DR, dos Santos AH, Dotto GL (2020) Efficient adsorbent based on construction and demolition wastes functionalized with 3-aminopropyltriethoxysilane (APTES) for the removal ciprofloxacin from hospital synthetic effluents. J Environ Chem Eng 8:1–7 10.1016/j.jece.2020.103875

Çok SS, Gizli N (2020) Hydrophobic silica aerogels synthesized in ambient conditions by preserving the pore structure via two-step silylation. Ceramics International 46:27789–27799 10.1016/j.ceramint.2020.07.278

637 Cunha MR, Lima EC, Lima DR, da Silva RS, Thue PS, Seliem MK, Sher F, dos Reis GS,
638 Larsson SH (2020) Removal of captopril pharmaceutical from synthetic pharmaceutical-
639 industry wastewaters: use of activated carbon derived from *Butia catarinensis*. J Environ
640 Chem Eng 8:1–9 10.1016/j.jece.2020.104506
641 de Oliveira Carvalho C, Rodrigues DLC, Lima EC, Umpierres CS, Caicedo DF, Machado FM
642 (2019) Kinetic, Equilibrium, and Thermodynamic Studies on the Adsorption of
643 Ciprofloxacin by Activated Carbon Produced from Jerivá (*Syagrus Romanzoffiana*).
644 Environmental Science and Pollution Research 26:4690–4702 10.1007/s11356-018-
645 3954-2
646 Desiraju GR, Ho PS, Kloo L, Legon AC, Marquardt R, Metrangolo P, Politzer P, Resnat G,
647 Rissanen K (2013) Definition of the halogen bond (IUPAC Recommendations 2013).
648 Pure Appl Chem 85:1711–1713 10.1351/PAC-REC-12-05-10
649 dos Reis GS, Guy M, Mathieu M, Jebrane M, Lima EC, Thyrel M, Dotto GL, Larsson SH (2022)
650 A comparative study of chemical treatment by $MgCl_2$, $ZnSO_4$, $ZnCl_2$, and KOH on
651 physicochemical properties and acetaminophen adsorption performance of biobased
652 porous materials from tree bark residues. Colloids Surf A: Physicochem Eng Aspects
653 642:1–13 10.1016/j.colsurfa.2022.128626
654 dos Reis GS, Sampaio CH, Lima EC, Wilhelm M (2016) Preparation of novel adsorbents based
655 on combinations of polysiloxanes and sewage sludge to remove pharmaceuticals from
656 aqueous solutions. Colloids Surf A: Physicochem Eng Aspects 497:304–315
657 10.1016/j.colsurfa.2016.03.021
658 Foroughi M, Khiadani M, Kakhki S, Kholghi V, Naderi K, Yektay S (2022) Effect of ozonation-
659 based disinfection methods on the removal of antibiotic-resistant bacteria and resistance
660 genes (ARB/ARGs) in water and wastewater treatment: a systematic review. Sci Total
661 Environ 811:1–23 10.1016/j.scitotenv.2021.151404
662 Goertzen SL, Theriault KD, Oickle AM, Tarasuk AC, Andreas HA (2010) Standardisation of
663 the Boehm titration. Part I. CO2 expulsion and endpoint determination. Carbon 48: 1252–
664 1261 10.1016/j.carbon.2009.11.050
665 Goertzen SL, Theriault KD, Oickle AM, Tarasuk AC, Andreas HA (2010) Standardisation of the
666 Boehm titration. Part I. CO_2 expulsion and endpoint determination. Carbon 48:1252–
667 1261.
668 Guellati A, Maachi R, Chaabane T, Darchen A, Danish M (2022) Aluminum dispersed bamboo
669 activated carbon production for effective removal of Ciprofloxacin hydrochloride
670 antibiotics: Optimization and mechanism study. J Environ Manage 301:1–11
671 10.1016/j.jenvman.2021.113765
672 Guy M, Mathieu M, Anastopoulos IP, Martínez MG, Rousseau F, Dotto GL, de Oliveira HP,
673 Lima EC, Thyrel M, Larsson SH, dos Reis GS (2022) Process Parameters Optimization,

674 Characterization, and Application of KOH-Activated Norway Spruce Bark Graphitic
675 Biochars for Efficient Azo Dye Adsorption. Molecules 27:1–25
676 10.3390/molecules27020456
677 Hagenbuch IM, Pinckney JL (2012) Toxic effect of the combined antibiotics ciprofloxacin,
678 lincomycin, and tylosin on two species of marine diatoms. Water Research 46:5028-
679 5036. 10.1016/j.watres.2012.06.040
680 Han L, Khalil AME, Wang J, Chen Y, Li F, Chang H, Zhang H, Liu X, Li G, Jia Q, Zhang S
681 (2022) Graphene-boron nitride composite aerogel: A high-efficiency adsorbent for
682 ciprofloxacin removal from water. Separation and Purification Technology 278:1–9
683 10.1016/j.seppur.2021.119605
684 Hanafy H, Li Z, Sellaoui L, Yazidi A, Wang H, Lima EC, Cimirro NFGM, Lamine AB, Erto A
685 (2021) Theoretical interpretation of the adsorption of amoxicillin on activated carbon via
686 physical model. Environmental Science and Pollution Research 28: 30714–30721
687 10.1007/s11356-021-12696-1
688 Igwegbe CA, Oba SN, Aniagor CO, Adeniyi AG, Ighalo JO (2021). Adsorption of ciprofloxacin
689 from water: A comprehensive review Journal of Industrial and Engineering Chemistry 93:
690 57–77 10.1016/j.jiec.2020.09.023
691 Jagiello J, Thommes M (2004) Comparison of DFT characterization methods based on N2, Ar,
692 CO2, and H2 adsorption applied to carbons with various pore size distributions. Carbon
693 42:1227–1232 10.1016/j.carbon.2004.01.022
694 Karoui S, Arfi RB, Mougin K, Ghorbal A, Assadi AA, Amrane A (2020) Synthesis of novel
695 biocomposite powder for simultaneous removal of hazardous ciprofloxacin and
696 methylene blue: Central composite design, kinetic and isotherm studies using Brouers-
697 Sotolongo family models. Journal of Hazardous Materials 387:1–17
698 10.1016/j.jhazmat.2019.121675
699 Khan NA, Najam T, Shah SSA, Hussain E, Ali H, Hussain S, Shaheen A, Ahmad K, Ashfaq M
700 (2020) Development of Mn-PBA on GO sheets for adsorptive removal of ciprofloxacin
701 from water: Kinetics, isothermal, thermodynamic, and mechanistic studies. Materials
702 Chemistry and Physics 245:1–11 10.1016/j.matchemphys.2020.122737
703 Kollarahithlu SC, Balakrishnan RM (2021) Adsorption of pharmaceuticals pollutants,
704 Ibuprofen, Acetaminophen, and Streptomycin from the aqueous phase using amine-
705 functionalized superparamagnetic silica nanocomposite. J Clean Prod 294:1–9
706 10.1016/j.jclepro.2021.126155
707 Kovtun A, Campodoni E, Favaretto L, Zambianchi M, Salatino A, Amalfitano S, Navacchia ML,
708 Casentini B, Palermo V, Sandri M, Melucci M (2020) Multifunctional graphene
709 oxide/biopolymer composite aerogels for microcontaminants removal from drinking
710 water. Chemosphere 259:1–10 10.1016/j.chemosphere.2020.127501

711 Kudo MVF, de Oliveira LLG, Suquila FAC, de Almeida FG, Segatelli MG, Lima EC, Dias SLP,
712 Tarley CRT (2020) Performance of Avocado Seed Activated Carbon as Adsorbent for
713 Highly Sensitive Determination of Cd Using a Flow Injection System Online Coupled to
714 TS-FF-AAS. J Brazilian Chem Soc 31:100–108 10.21577/0103-5053.20190132
715 Lam VT, Ngo TCQ, Bach LG (2021) Facile Fabrication of Novel $NiFe_2O_4$@Carbon Composites
716 for Enhanced Adsorption of Emergent Antibiotics. Materials 14:1–21
717 10.3390/ma14216710
718 Lawal IA, Klink M, Ndungu P (2019) Deep eutectic solvent as an efficient modifier of low-cost
719 adsorbent for the removal of pharmaceuticals and dye. Environmental Research 179:1–
720 11 10.1016/j.envres.2019.108837
721 Leite AJB, Saucier C, Lima EC, dos Reis GS, Umpierres CS, Mello BL, Shirmardi M, Dias SLP,
722 Sampaio CH (2018) Activated carbons from avocado seed: Optimization and application
723 for removal several emerging organic compounds. Environ Sci Pollut Res 25:7647–7661
724 10.1007/s11356-017-1105-9
725 Leite AJB, Sophia AC, Thue PS, dos Reis GS, Dias SLP, Lima EC, Vaghetti JCP, Pavan FA,
726 de Alencar WS (2017) Activated carbon from avocado seeds for the removal of phenolic
727 compounds from aqueous solutions. Desalin Water Treat 71:168–181
728 10.5004/dwt.2017.20540
729 Li H, Song R, Wang Y, Zhong R, Zhang Y, Zhou J, Wang T, Zhu L (2021) Simultaneous
730 removal of antibiotic-resistant bacteria and its resistance genes in water by plasma
731 oxidation: Highlights the effects of inorganic ions. Sep Purif Technol 278:1–9
732 10.1016/j.seppur.2021.119672
733 Lima DR, Hosseini-Bandegharaei A, Thue PS, Lima EC, de Albuquerque YRT, dos Reis GS,
734 Umpierres CS, Dias SLP, Tran HN (2019a) Efficient acetaminophen removal from water
735 and hospital effluents treatment by activated carbons derived from Brazil nutshells.
736 Colloid Surf A 583:1–12 10.1016/j.colsurfa.2019.123966
737 Lima DR, Lima EC, Umpierres CS, Thue PS, El-Chaghaby GA, da Silva RS, Pavan FA, Dias
738 SP, Biron C (2019b) Removal of amoxicillin from simulated hospital effluents by
739 adsorption using activated carbons prepared from capsules of cashew of Para. Environ
740 Sci Pollut Res 26:16396–16408 10.1007/s11356-019-04994-6
741 Lima EC, Dehghani MH, Guleria A, Sher F, Karri RR, Dotto GL, Tran HN (2021a) Adsorption:
742 Fundamental aspects and applications of adsorption for effluent treatment. In: Dehghani
743 MH, Karri R, Lima EC (eds.) Green Technologies for the Defluoridation of Water.
744 Elsevier, pp 41–88 Doi: 10.1016/b978-0-323-85768-0.00004-x
745 Lima EC, Gomes AA, Tran HN (2020) Comparison of the nonlinear and linear forms of the
746 van't Hoff equation for calculation f adsorption thermodynamic parameters ($\Delta S°$ and
747 $\Delta H°$). J. Mol Liq 311:1–6 10.1016/j.molliq.2020.113315

748 Lima EC, Hosseini-Bandegharaei A, Anastopoulos I (2019b) Response to “Some remarks on
749 a critical review of the estimation of the thermodynamic parameters on adsorption
750 equilibria. Wrong use of equilibrium constant in the van’t Hoff equation for calculation of
751 thermodynamic parameters of adsorption - Journal of Molecular Liquids 273 (2019) 425–
752 434”. J Mol Liq 280:298–300 10.1016/j.molliq.2019.01.160
753 Lima EC, Hosseini-Bandegharaei A, Moreno-Piraján JC, Anastopoulos I (2019a) A critical
754 review of the estimation of the thermodynamic parameters on adsorption equilibria.
755 Wrong use of equilibrium constant in the Van’t Hoff equation for calculation of
756 thermodynamic parameters of adsorption. J Mol Liq 273:425–434
757 10.1016/j.molliq.2018.10.048
758 Lima EC, Sher F, Guleria A, Saeb MR, Anastopoulos I, Tran HN, Hosseini-Bandegharaei A
759 (2021b) Is one performing the treatment data of adsorption kinetics correctly? J. Environ.
760 Chem Eng 9:1–9 10.1016/j.jece.2020.104813
761 Ma L, Liu Y, Yang Q, Jiang L, Li G (2022) Occurrence and distribution of Pharmaceuticals and
762 Personal Care Products (PPCPs) in wastewater-related riverbank groundwater. Sci.
763 Total Environ 82:1–10 10.1016/j.scitotenv.2022.153372
764 Magesh N, Annam Renita A, Siva R, Harirajan N, Santhosh A (2022) Adsorption behavior of
765 fluoroquinolone(ciprofloxacin) using zinc oxide impregnated activated carbon prepared
766 from jack fruit peel: Kinetics and isotherm studies. Chemosphere 290:1–10
767 10.1016/j.chemosphere.2021.133227
768 Najafpoor AA, Sani ON, Alidadi H, Yazdani M, Fezabady AAN, Taghavi M (2019) Optimization
769 of ciprofloxacin adsorption from synthetic wastewaters using γ-Al_2O_3 nanoparticles: An
770 experimental design based on response surface methodology. Colloid and Interface
771 Science Communications 33:1–7 10.1016/j.colcom.2019.100212
772 Nie XP, Liu BY, Yu HJ, Liu WQ, Yang YF (2013) Toxic effects of erythromycin, ciprofloxacin
773 and sulfamethoxazole exposure to the antioxidant system in Pseudokirchneriella
774 subcapitata. Environmental Pollution 172: 23-32 10.1016/j.envpol.2012.08.013.
775 Oickle AM, Goertzen SL, Hopper KR, Abdalla YO, Andreas HA (2010) Standardisation of the
776 Boehm titration: Part II. Method of agitation, the effect of filtering, and dilute titrant.
777 Carbon 48:3313–3322 10.1016/j.carbon.2010.05.004
778 Oickle AM, Goertzen SL, Hopper KR, Abdalla YO, Andreas HA (2010) Standardisation of the
779 Boehm titration: Part II. Method of agitation, the effect of filtering, and dilute titrant.
780 Carbon 48: 3313-3322.
781 Panahi AH, Ashrafi SD, Kamani H, Khodadadi M, Lima, EC, Mostafapour FK, Mahvi AH (2019)
782 Removal of cephalexin from artificial wastewater by mesoporous silica materials using
783 Box-Behnken response surface methodology. Desalin Water Treat 159:169–180
784 10.5004/dwt.2019.24109

Qiu W, Sun J, Fang M, Luo S, Tian Y, Dong P, Xu B, Zheng C (2019) Occurrence of antibiotics in the main rivers of Shenzhen, China: Association with antibiotic resistance genes and microbial Community. Sci Total Environ 653:334–341 10.1016/j.scitotenv.2018.10.398

Rahman N, Varshney P (2021) Facile Synthesis and Characterization of Zn(II)-Impregnated Chitosan/Graphene Oxide: Evaluation of Its Efficiency for Removal of Ciprofloxacin from Aqueous Solution. Journal of Inorganic and Organometallic Polymers and Materials 31:3595–3612 10.1007/s10904-021-01981-8

Sadredinamin M, Shabani M, Karimi A, Sohrabi MR, Karimi-Yazdi M, Ghalavand Z, Alebouyeh M (2022) Virulence genes expression profiling of different *Shigella flexneri* serotypes in response to sub-inhibitory concentrations of azithromycin and ciprofloxacin. Gut Pathogens 14:10. 10.1186/s13099-022-00483-3.

Sellaoui L, Dhaouadi F, Taamalli S, AlZahrani HYS, Louis F, El-Bakali A, Erto A, Lamine AB, Lima DR, Lima EC, Chen Z (2022) Application of a multilayer physical model for the critical analysis of the adsorption of nicotinamide and propranolol on magnetic-activated carbon. Environmental Science and Pollution Research (2022) 29:30184–30192 10.1007/s11356-021-18483-2

Sellaoui L, Kehili M, Lima EC, Thue PS, Bonilla-Petriciolet A, Lamine AB, Dotto GL, Erto A. (2019) Adsorption of phenol on microwave-assisted activated carbons: Modelling and interpretation. Journal of Molecular Liquids 274: 309–314 10.1016/j.molliq.2018.10.098

Sellaoui L, Mechi N, Lima EC, Dotto GL, Lamine AB (2017) Adsorption of diclofenac and nimesulide on activated carbon: Statistical physics modeling and effect of adsorbate size. Journal of Physics and Chemistry of Solids 109: 117–123 10.1016/j.jpcs.2017.05.019

Sellaoui L, Yazidi A, Taamalli A, Bonilla-Petriciolet A, Louis F, El-Bakali A, Badawi M, Lima EC, Lima DR, Chen Z (2021) Adsorption of 3-aminophenol and resorcinol on avocado seed activated carbon: Mathematical modelling, thermodynamic study and description of adsorbent performance. Journal of Molecular Liquids 342 (2021) 116952 10.1016/j.molliq.2021.116952

Sophia CA, Lima EC (2018) Removal of emerging contaminants from the environment by adsorption. Ecotoxicol Environ Saf 150 1–17 10.1016/j.ecoenv.2017.12.026

STATISTA (2020). Production of avocado in Brazil from 2013 to 2019. https://www.statista.com/statistics/934976/brazil-avocado-production-volume/. The website was visited on February 19th, 2022.

Teixeira RA, Lima EC, Benetti AD, Thue PS, Cunha MR, Cimirro NFGM, Sher F, Dehghani MH, dos Reis GS, Dotto GL (2021) Preparation of hybrids of wood sawdust with 3-aminopropyltriethoxysilane. Application as an adsorbent to remove Reactive Blue 4 dye from wastewater effluents. Journal of the Taiwan Institute of Chemical Engineers

125:141–152 10.1016/j.jtice.2021.06.007

Thommes M, Kaneko K, Neimark AV, Olivier JP, Rodriguez-Reinoso FJ, Rouquerol KS, Sing W (2015) Physisorption of gases, with special reference to the evaluation of surface area and pore size distribution (IUPAC Technical Report). Pure Appl Chem 87:1051–1069 10.1515/pac-2014-1117

Thue PS, Lima EC, Sieliechi JM, Saucier C, Dias SLP, Vaghetti JCP, Rodembusch FS, Pavan FA (2017) Effects of first–row transition metals and impregnation ratios on the physicochemical properties of microwave-assisted activated carbons from wood biomass. J Colloid Interface Sci 486:163–175 10.1016/j.jcis.2016.09.070

Thue PS, Umpierres CS, Lima EC, Lima DR, Machado FM, dos Reis GS, da Silva RS, Pavan FA, Tran HN (2020) Single-step pyrolysis for producing magnetic activated carbon from tucumã (Astrocaryum aculeatum) seed and nickel(II) chloride and zinc(II) chloride. Application for removal of Nicotinamide and Propanolol. J Hazard Mater 398:1–13 10.1016/j.jhazmat.2020.122903

Tian Y, Yao S, Zhou L, Hu Y, Lei J, Wang L, Zhang J, Liu Y, Cui C (2022) Efficient removal of antibiotic-resistant bacteria and intracellular antibiotic resistance genes by heterogeneous activation of peroxymonosulfate on hierarchical macro-mesoporous Co3O4-SiO2 with enhanced photogenerated charges. J Hazard Mater 430:1–10 10.1016/j.jhazmat.2021.127414

Tomul F, Arslan Y, Kabak B, Trak D, Kendüzler E, Lima EC, Tran HN (2020) Peanut shells-derived biochars prepared from different carbonization processes: Comparison of characterization and mechanism of naproxen adsorption in water. Sci Total Environ 726:1–16 10.1016/j.scitotenv.2020.137828

Wamba AGN, Lima EC, Ndi SK, Thue PS, Kayem JG, Rodembusch FS, dos Reis GS, de Alencar WS (2017) Synthesis of grafted natural pozzolan with 3-aminopropyltriethoxysilane: Preparation, characterization, and application for removal of Brilliant Green 1 and Reactive Black 5 from aqueous solutions. Environ Sci Pollut Res 24:21807–21820 10.1007/s11356-017-9825-4

Wang Q, Yang M, Qi X, Wang J, Sun K, Li Z, Deng G (2021) A novel graphene oxide decorated with halloysite nanotubes (HNTs/GO) composite used for the removal of levofloxacin and ciprofloxacin in a wide pH range. New J Chem 45:1–12 10.1039/d1nj03807a

Wang R, Ji M, Zhai H, Guo Y, Liu Y (2021) Occurrence of antibiotics and antibiotic resistance genes in WWTP effluent-receiving water bodies and reclaimed wastewater treatment plants. Sci Total Environ 796:1–12 10.1016/j.scitotenv.2021.148919

Wang Y, Wei W, Lin Y, Zhang M, Wang Y, Liu M (2020) Assembly of SPS/MgSi assisted by dopamine with excellent removal performance for ciprofloxacin. Journal of Environmental Sciences 94:111–118 10.1016/j.jes.2020.03.016

Wu G, Ma J, Li S, Guan J, Jiang B, Wang L, Li J, Wang X, Chen L (2018) Magnetic copper-based metal-organic framework as an effective and recyclable adsorbent for removal of two fluoroquinolone antibiotics from aqueous solutions. Journal of Colloid and Interface Science 528:360–371 10.1016/j.jcis.2018.05.105

Wu Y, Zheng H, Li H, Sun Y, Zhao C, Zhao R, Zhang C (2021) Magnetic nickel-cobalt sulfide/sodium dodecyl benzene sulfonate with excellent ciprofloxacin adsorption capacity and wide pH adaptability. Chem Eng J 426:1–9 10.1016/j.cej.2020.127208

Xikhongelo RV, Mtunzi FM, Diagboya PN, Olu-Owolabi BI, Düring RA (2021) Polyamidoamine-Functionalized Graphene Oxide−SBA-15 Mesoporous Composite: Adsorbent for Aqueous Arsenite, Cadmium, Ciprofloxacin, Ivermectin, and Tetracycline. Ind Eng Chem Res 60:3957–3968 10.1021/acs.iecr.0c04902

Yadav A, Asthana A, Singh AK, Chakraborty R, Vidya SS, Susan MABH, Carabineiro SAC (2021) Adsorption of cationic dyes, drugs, and metal from aqueous solutions using a polymer composite of magnetic/β-cyclodextrin/activated charcoal/Na alginate: Isotherm, kinetics and regeneration studies. J Hazard Mater 409:1–22 10.1016/j.jhazmat.2020.124840

Yang Q, Yu H, He Y, Liu Z, Qin C, Liu B, Li Y (2020) Porous three-component hybrid hydrogen-bonded covalent organic polymers: Design, synthesis and ciprofloxacin adsorption. European Polymer Journal 123:1–10 10.1016/j.eurpolymj.2019.109445

Yazidi A, Sellaoui L, Badawi M, Lima EC, Bonilla-Petriciolet A, Thue PS, Cimirro NFGM, Lamine AB (2020) Physicochemical interpretation of the adsorption of 4-Bromophenol and 4-Chloroaniline on activated carbon. Journal of Environmental Chemical Engineering 8 (2020) 104542 10.1016/j.jece.2020.104542

Yu D, He J, Xie T, Xu Q, Li G, Du L, Huang J, Yang J, Li W, Wang J (2022) Peroxymonosulfate activation using a composite of copper and nickel oxide coated on SBA-15 for the removal of sulfonamide antibiotics. Environ Res 206:1–11 10.1016/j.envres.2021.112301

Yu F, Chen D, Ma J (2018) Adsorptive removal of ciprofloxacin by ethylenediaminetetraacetic acid/b-cyclodextrin composite from aqueous solution. New J Chem 42:1–8 10.1039/c7nj03770h

List of Tables

Table 1. CHN/O elemental analysis, HI, total acidity and total basicity, and pHpzc for R_1 and R_2 composites.

	C (%)	H (%)	N (%)	O(%)	Ashes(%)	Total Acidity (mmol g^{-1})	Total Basicity (mmol g^{-1})	HI	pH_{pzc}
R1	53.64	3.76	1.05	11.28	30.27	0.1025	0.1056	1.725	5.09
R2	61.22	3.01	1.14	8.00	26.63	0.2617	0.3125	1.051	4.91

Table 2. Kinetic parameters for adsorption of CIP onto R_1 and R_2 composite adsorbents. Conditions: C_o =100 mg L^{-1}; T= 25°C, the adsorbent dosage = 1.5 g L^{-1}, pH = 7. All values are expressed with four significant digits

	R_1	R_2
Pseudo-first order		
q_e (mg g^{-1})	6.208	41.41
k_1 (min^{-1})	0.03993	0.05762
$t_{1/2}$ (min)	17.36	12.03
$t_{0.95}$ (min)	75.02	52.00
R^2 adjusted	0.9133	0.9536
SD (mg g^{-1})	0.6522	3.231
BIC	-12.34	61.27
Pseudo-second order		
q_e (mg g^{-1})	6.812	45.11
k_2 (g mg^{-1} min^{-1})	0.008730	0.001759
$t_{1/2}$ (min)	15.38	11.78
$t_{0.95}$ (min)	165.2	140.9
R^2 adjusted	0.9670	0.9905
SD (mg g^{-1})	0.4025	1.459
BIC	-34.54	24.70
Avrami-fractional-order		
q_e (mg g^{-1})	7.677	44.87
K_{AV} (min^{-1})	0.01672	0.03720
n_{AV}	0.4750	0.5851
$t_{1/2}$ (min)	20.52	14.00
$t_{0.95}$ (min)	246.4	157.6
R^2 adjusted	0.9999	0.9975
SD (mg g^{-1})	0.02070	0.7514
BIC	-169.1	-3.818

Table 3. Langmuir, Freundlich, and Liu isotherm parameters for CIP adsorption on R_1 and R_2 adsorbents. Adsorbent dosage = 1.5 g L^{-1}, pH = 7.0. Time of contact between CIP and adsorbent, 300 min R_1, 180 min R_2. All values are expressed with four significant digits.

R_1						
	10°C	**20°C**	**25°C**	**30°C**	**40°C**	**45°C**
Langmuir						
Q_{max} (mg g^{-1})	11.18	5.102	49.95	12.12	17.41	5.001
K_L (L mg^{-1})	0.01522	0.2043	0.001427	0.007966	0.003419	7.631
R^2_{adj}	0.9861	0.9446	0.8904	0.9986	0.9975	0.8964
SD (mg g^{-1})	0.3330	0.3653	1.135	0.08957	0.1019	0.4518
BIC	-29.00	-26.05	10.24	-71.03	-66.90	-19.27
Freundlich						
K_F(mg.g^{-1}.(mg.L^{-1})$^{-1/nF}$)	0.5800	1.947	0.08481	0.2894	0.1156	3.666
n_F	1.909	5.070	1.078	1.600	1.270	12.69
R^2_{adj}	0.9441	0.9955	0.8815	0.9855	0.9916	0.9992
SD (mg g^{-1})	0.6682	0.1037	1.180	0.2868	0.1856	0.03861
BIC	-6.721	-66.33	11.48	-33.78	-47.72	-97.95
Liu						
Q_{max} (mg g^{-1})	8.411	8.850	9.326	9.838	10.21	10.77
K_g (L mg^{-1})	0.02589	0.01768	0.01459	0.01203	0.008371	0.007120
n_L	1.630	0.3473	4.205	1.193	1.288	0.1331
R^2_{adj}	0.9999	0.9999	0.9999	0.9999	0.9999	0.9999
SD (mg g^{-1})	0.009476	0.003567	0.01933	0.004233	0.02030	$4.384.10^{-4}$
BIC	-141.3	-172.6	-118.5	-167.1	-116.9	-239.7

909 **Table 3**. Continuation.

R_2						
	10°C	**20°C**	**25°C**	**30°C**	**40°C**	**45°C**
Langmuir						
Q_{max} (mg g^{-1})	53.00	63.35	60.27	71.40	92.66	131.7
K_L (L mg^{-1})	0.1641	0.08369	0.08102	0.05270	0.02532	0.01340
R^2_{adj}	0.9989	0.9893	0.9993	0.9898	0.9712	0.9656
SD (mg g^{-1})	0.5614	2.094	0.4748	2.058	4.033	4.284
BIC	-12.30	29.83	-17.66	29.28	50.81	52.74
Freundlich						
K_F(mg.g^{-1}.(mg.L^{-1})$^{-1/nF}$)	16.17	12.27	12.26	9.314	4.958	3.080
n_F	3.920	2.861	2.980	2.332	1.701	1.386
R^2_{adj}	0.9453	0.9109	0.9416	0.9333	0.9286	0.9438
SD (mg g^{-1})	3.991	6.032	4.361	5.265	6.348	5.479
BIC	50.47	63.99	53.31	59.34	65.32	60.61
Liu						
Q_{max} (mg g^{-1})	54.69	56.45	58.18	60.01	61.85	63.80
K_g (L mg^{-1})	0.1517	0.1045	0.08729	0.07353	0.05227	0.04414
n_L	0.8947	1.478	1.098	1.486	2.061	2.411
R^2_{adj}	0.9999	0.9999	0.9999	0.9999	0.9999	0.9999
SD (mg g^{-1})	0.003858	0.003098	0.04694	0.1754	0.05048	0.1115
BIC	-170.1	-177.1	-90.12	-47.94	-87.79	-62.42

910

911

912

913 **Table 4**. Adsorbents utilized for removal of CIP.

Adsorbent	Q_{max} (mg g^{-1})	Ref
Aluminum dispersed bamboo activated carbon	13.36	Guellati et al., 2022
Chitosan-gelatin-graphene oxide aerogels	8.4	Kovtun et al., 2020
Zinc oxide impregnated activated carbon	15.75	Magesh et al., 2022
Carbon dioxide activated biochar-clay mineral composite	50.32	Arif et al., 2022
Jerivá activated carbon	198.6-335.8	de Oliveira Carvalho et al., 2010
Demolition wastes modified with APTES	98.9-138.0	Caicedo et al., 2020
A polymer composite of magnetic/β-cyclodextrin/activated charcoal/Na alginate	3.125	Yadav et al., 2021
Graphene oxide decorated with halloysite nanotubes (HNTs/GO) composite	467.3-943.4	Wang, Q et al., 2021
Biochar–clay hybrid adsorbent	140.3	Lawal et al., 2019
Ethylenediaminetetraacetic acid/β-cyclodextrin composite	448	Yu et al., 2018
Metal-organic-framework	1826	Khan et al., 2020
γ -Al_2O_3 nanoparticles	5.12	Najafpoor et al., 2019
Graphene-boron nitride composite aerogel	185	Han et al., 2022
Copper-based metal-organic framework	538	Wu et al., 2018
Magnesium silicate-based sulfonated polystyrene sphere composites	329.7	Wang et al., 2020;
Magnetic nickel cobalt sulfide/sodium dodecyl benzene sulfonate	625	Wu et al., 2021
$NiFe_2O_4$@Carbon Composites	737.42	Lam et al. 2021
Polyamidoamine-Functionalized Graphene Oxide – SBA-15	24.6	Xikhongelo et al., 2021
Hybrid hydrogen-bonded covalent organic polymers	84.03	Yang et al., 2020
Zn(II)-Impregnated Chitosan/Graphene Oxide	211.5-227.6	Rahman et al., 2021
Biocomposite of regenerated-reed plus reed-charcoal	31.8	Karoui et al., 2020
R_1	8.41-10.77	This work
R_2	54.69-63.80	This work

914

915

916

917

918 **Table 5.** Thermodynamic parameters of the adsorption of CIP on R_1 and R_2 adsorbents. All

919 values are expressed with four significant digits.

Temperature (K)	**283**	**293**	**298**	**303**	**313**	**318**
Liu model						
R_1						
K_e^0	$8.578.10^3$	$5.857.10^3$	$4.835.10^3$	$3.985.10^3$	$2.774.10^3$	$2.359.10^3$
ΔG^0 (kJ mol^{-1})	-21.31	-21.13	-21.02	-20.88	-20.63	-20.53
ΔH^0 (kJ mol^{-1})	-	-	-27.42	-	-	-
ΔS^0 (J K^{-1} mol^{-1})	-	-	-21.54	-	-	-
R^2	-	-	0.9996	-	-	-
R^2_{adj}	-	-	0.9995	-	-	-
Liu model						
R_2						
K_e^0	$5.026.10^4$	$3.463.10^4$	$2.892.10^4$	$2.436.10^4$	$1.732.10^4$	$1.462.10^4$
ΔG^0 (kJ mol^{-1})	-25.47	-25.46	-25.45	-25.45	-25.40	-25.36
ΔH^0 (kJ mol^{-1})	-	-	-26.10	-	-	-
ΔS^0 (J K^{-1} mol^{-1})	-	-	-2.195	-	-	-
R^2	-	-	0.9999	-	-	-
R^2_{adj}	-	-	0.9998	-	-	-

920

921

922

Captions for Figures

Fig 1. Textural characteristics of R_1 and R_2 samples. (a) isotherm of adsorption of R_1; (b) pore size distribution of R_1; (c) isotherm of adsorption of R_2; (d) pore size distribution of R_2.

Fig 2. FTIR spectra (a) R_1, (b) R_2.

Fig 3. Raman spectra.

Fig 4. TGA analysis (a) R_1, (b) R_2. From room temperature up to 800°C, the gas utilized was N_2. From 800° to 1000°C, the gas utilized was synthetic air.

Fig 5. Kinetic Curves for CIP adsorption onto (a) R1; and (b) R2 composite adsorbents. Conditions: the initial CIP concentration was 100 mg L^{-1}, the temperature was fixed at 25°C, the adsorbent dosage of 1.5 g L^{-1}, initial pH of the adsorbate solution was 7.0.

Fig 6. Isotherms of adsorption of CIP on R1 adsorbent. (a) 10°C; (b) 20°C; (c) 25°C; (d) 30°C; (e) 40°C; (f) 45°C. Conditions: time of contact 300 min between CIP and R_1; adsorbent dosage 1.5 g.L^{-1}; initial pH 7.0.

Fig 7. Isotherms of adsorption of CIP on R_2 adsorbent. (a) 10°C; (b) 20°C; (c) 25°C; (d) 30°C; (e) 40°C; (f) 45°C. Conditions: time of contact 180 min between CIP and R_2; adsorbent dosage 1.5 g.L^{-1}; initial pH 7.0.

Fig 8. Nonlinear van´t Hoff equation for ciprofloxacin uptake by (a) R_1; (b) R_2 adsorbents.

Fig 9. Schematic representation of interaction mechanism of ciprofloxacin and biochar@MK composites.

List of Figures

Figures 1

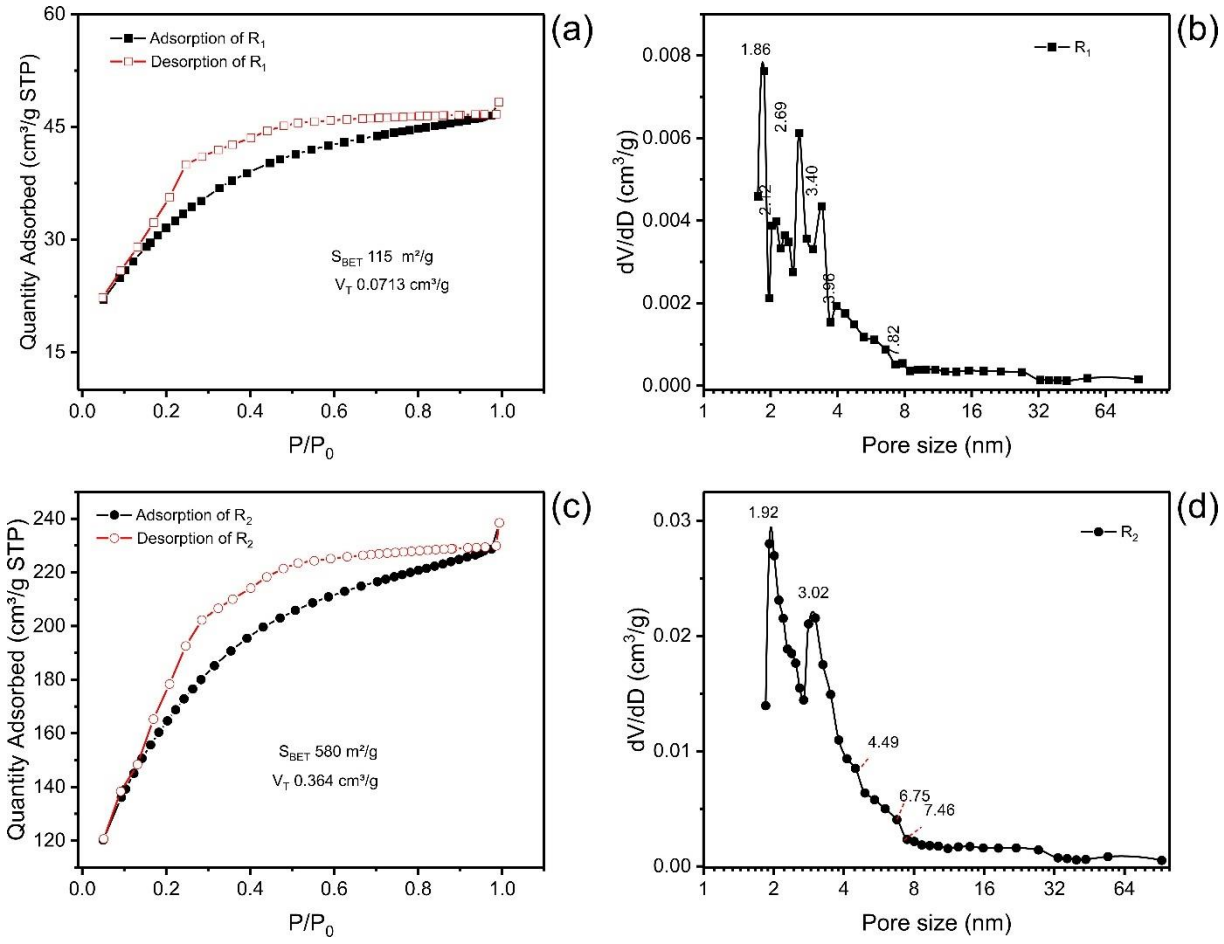

957 **Figures 2**

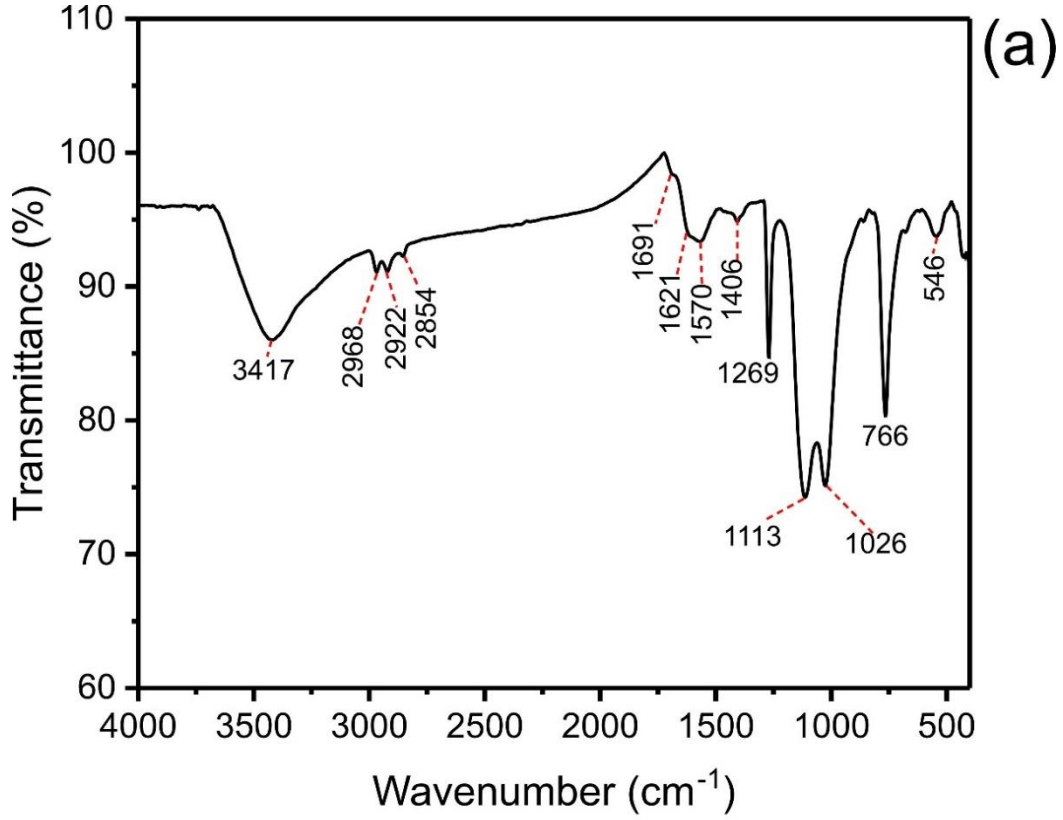

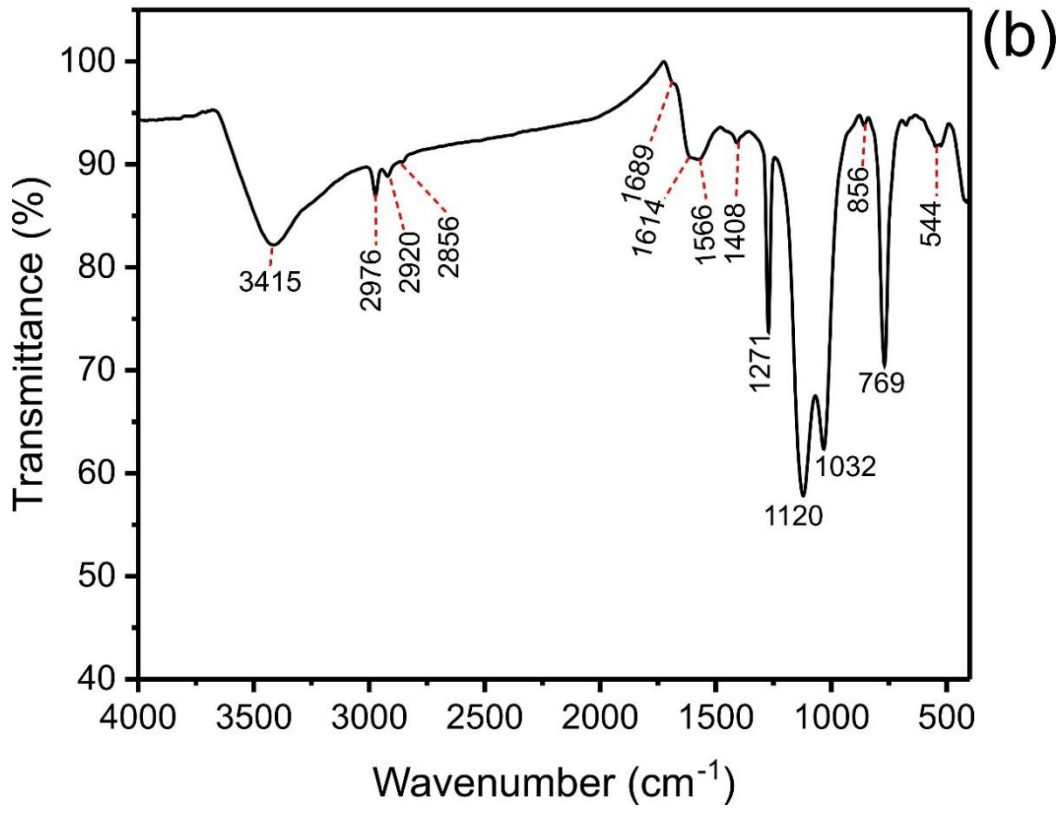

958

959

960 **Figures 3**

961

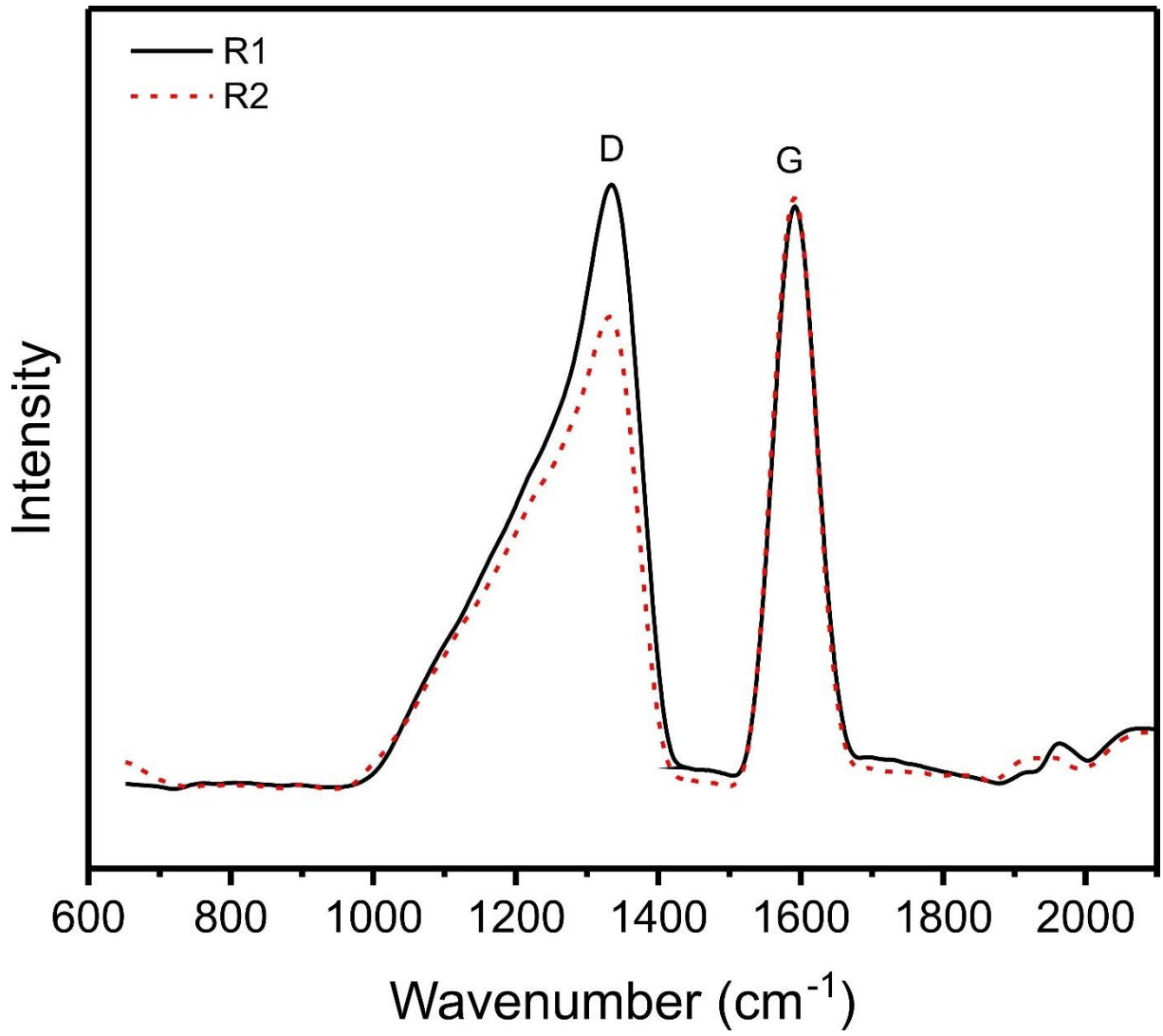

962

963

964 **Figures 4**

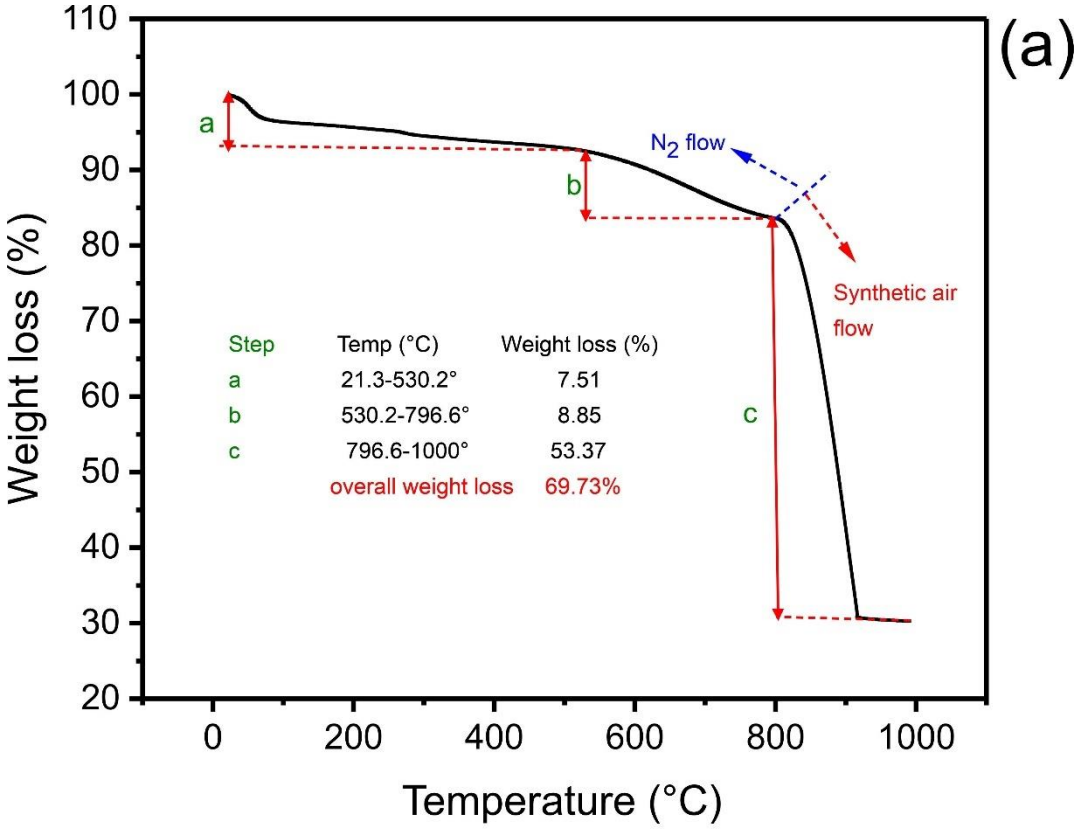

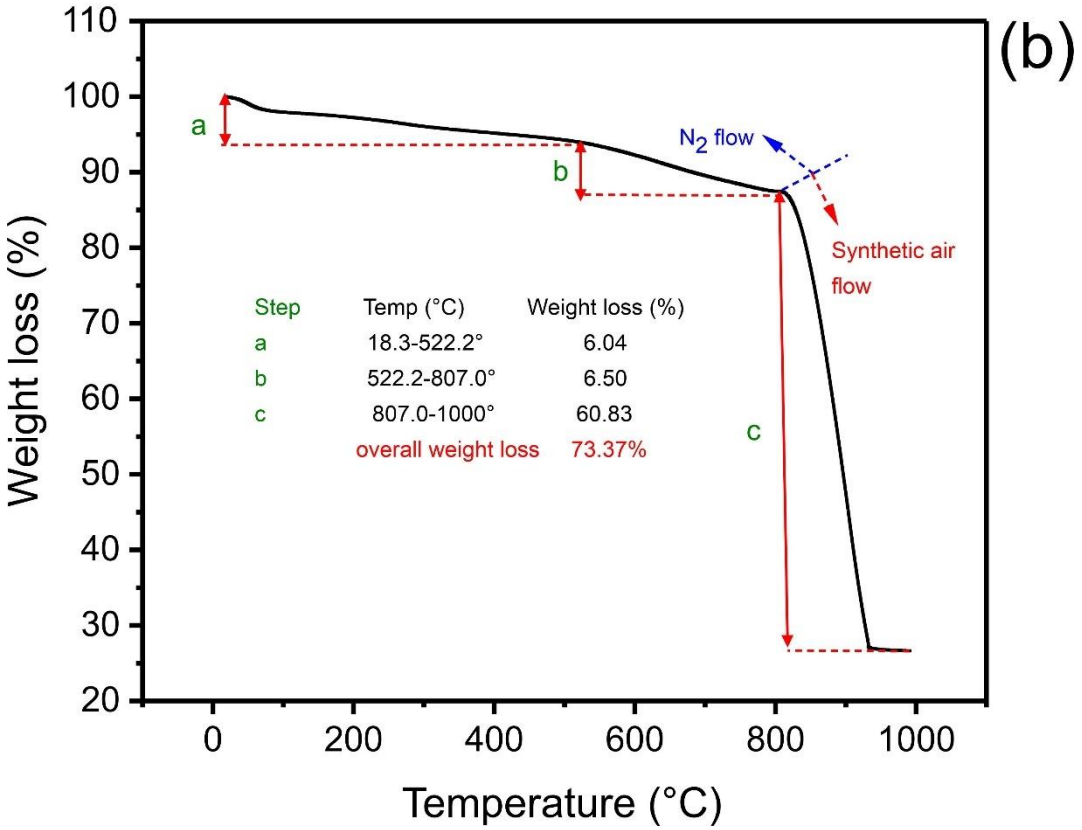

965

966

967 **Figures 5**

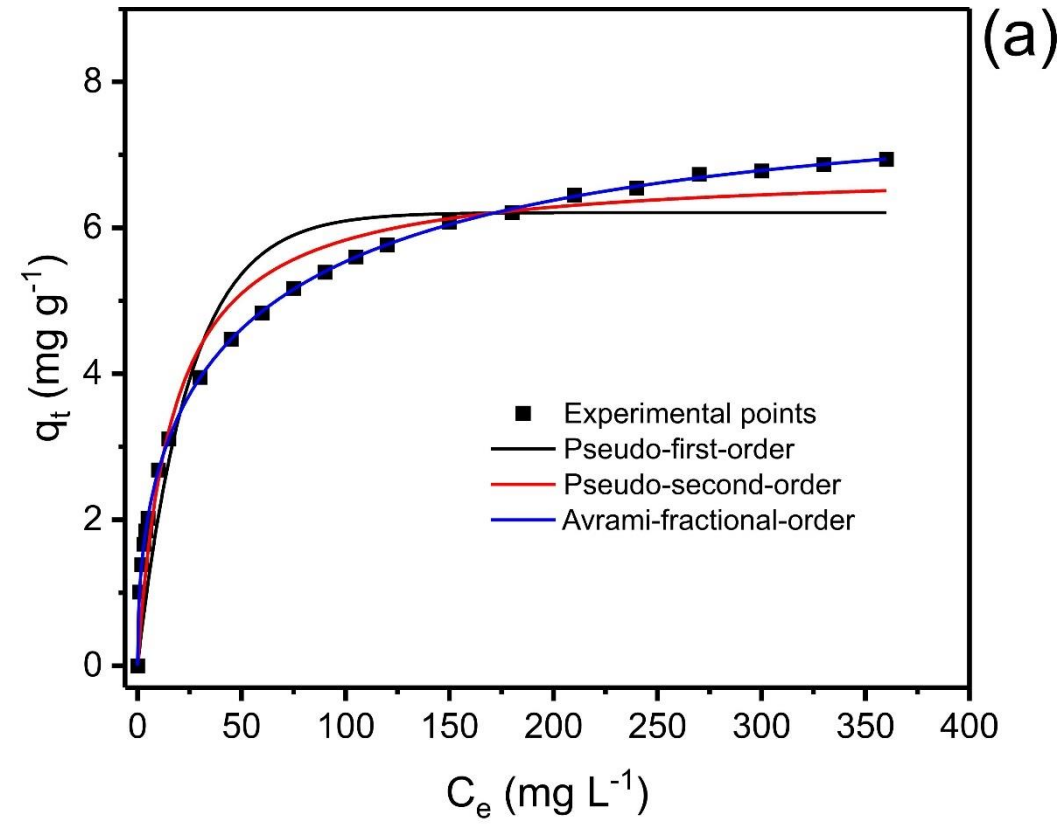

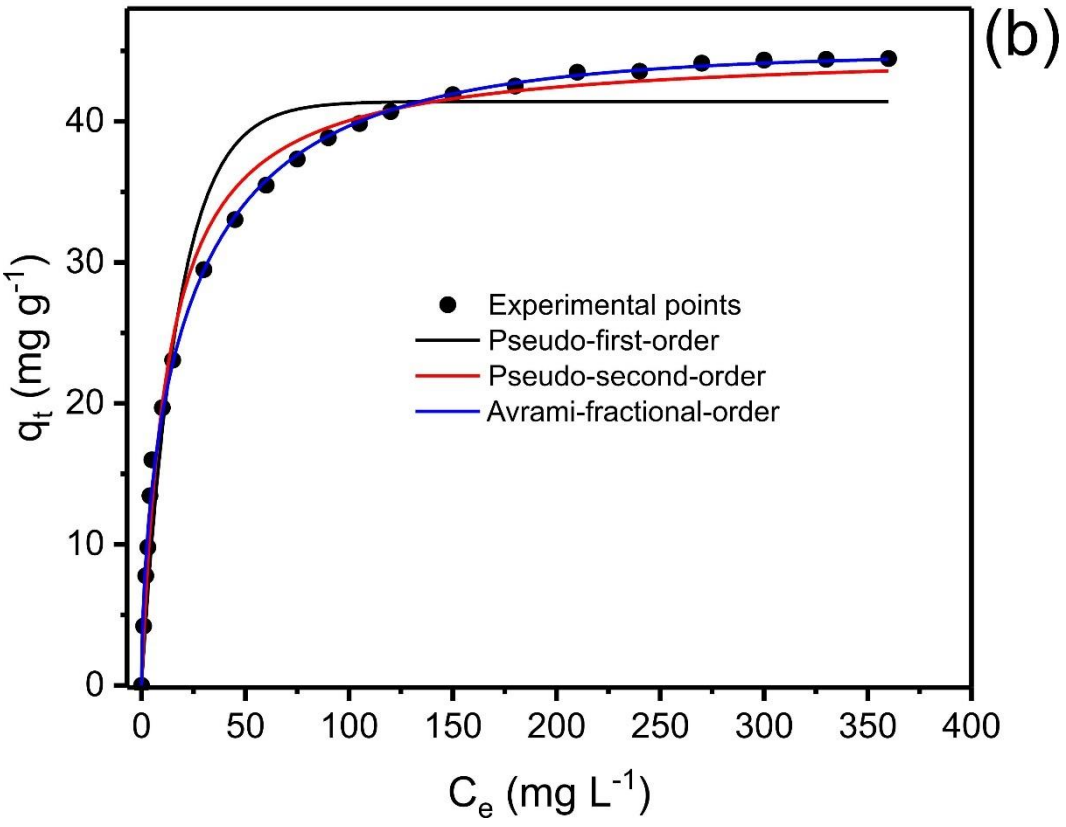

968

969 **Figures 6**

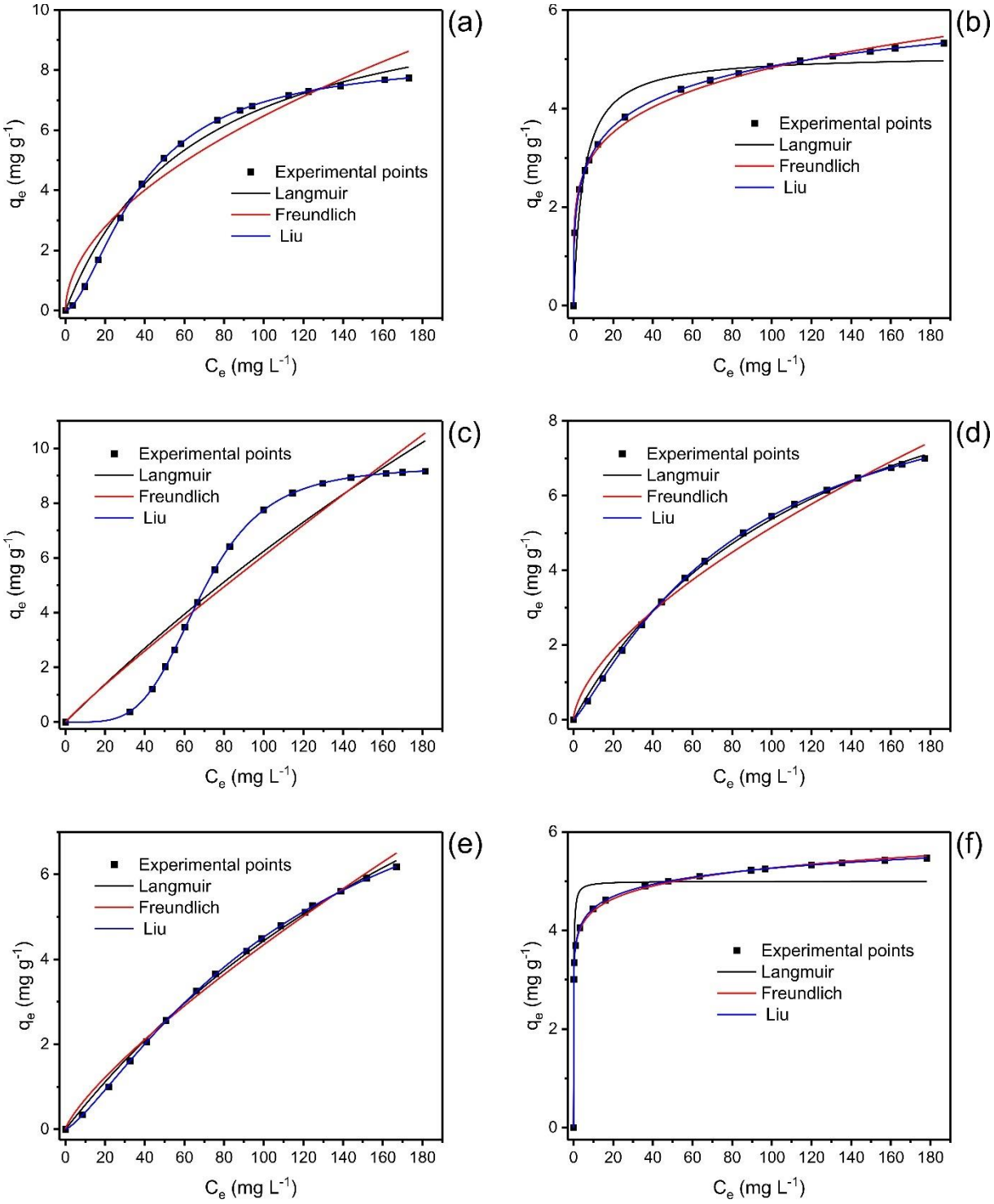

970

971

Figures 7

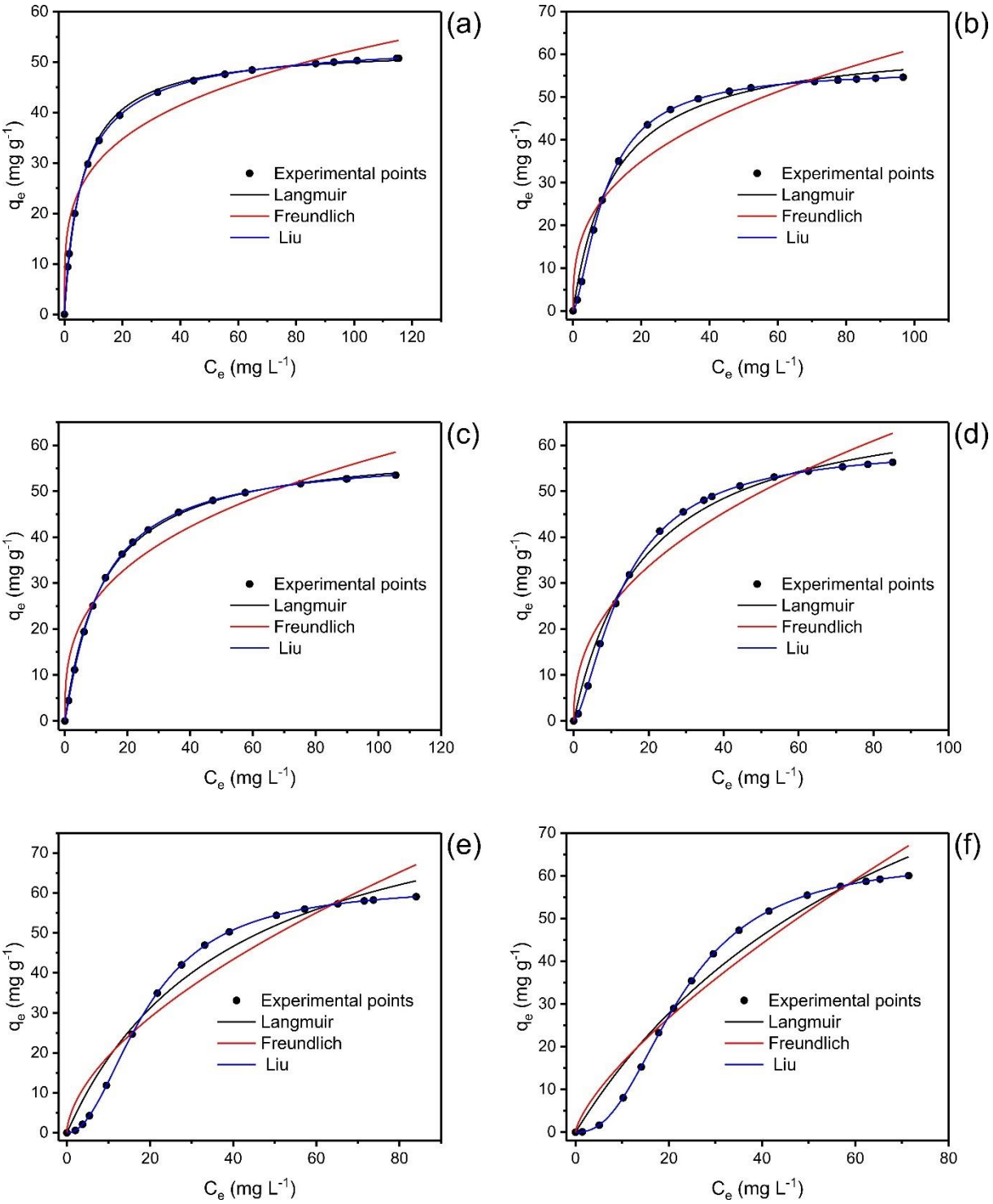
(a)
(b)
(c)
(d)
(e)
(f)
Experimental points
Langmuir
Freundlich
Liu
q_e (mg g^{-1})
C_e (mg L^{-1})

976 **Figures 8**

977

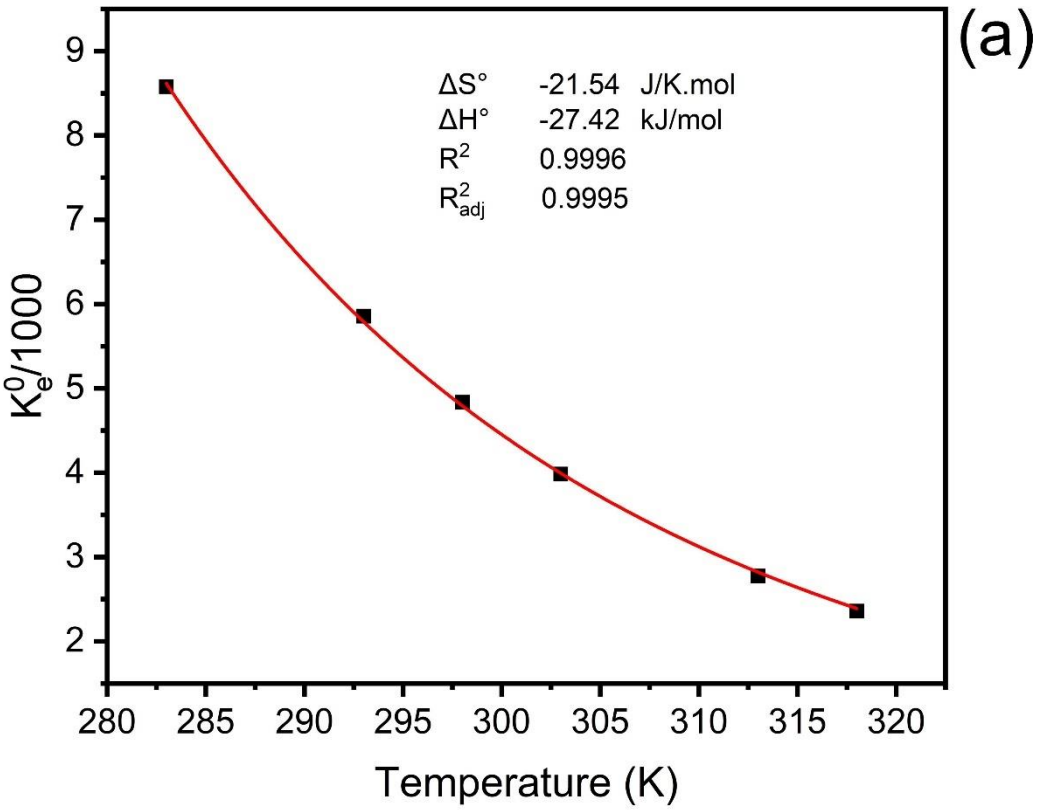

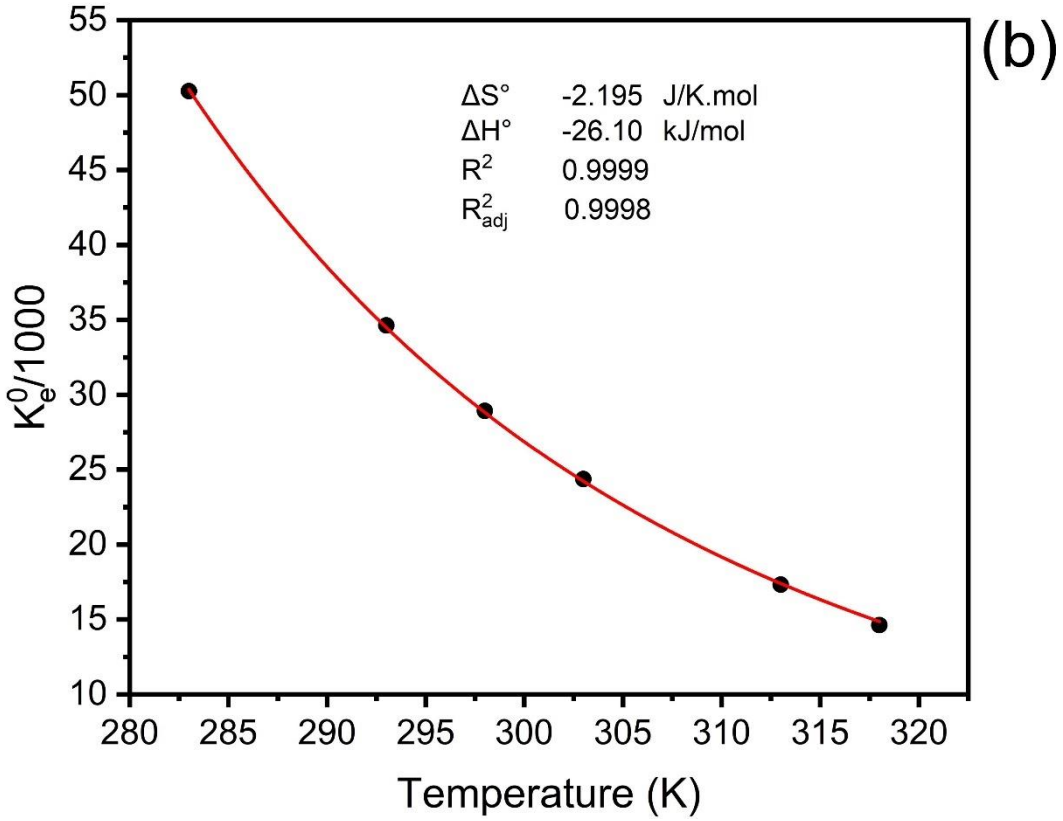

978

Figures 9

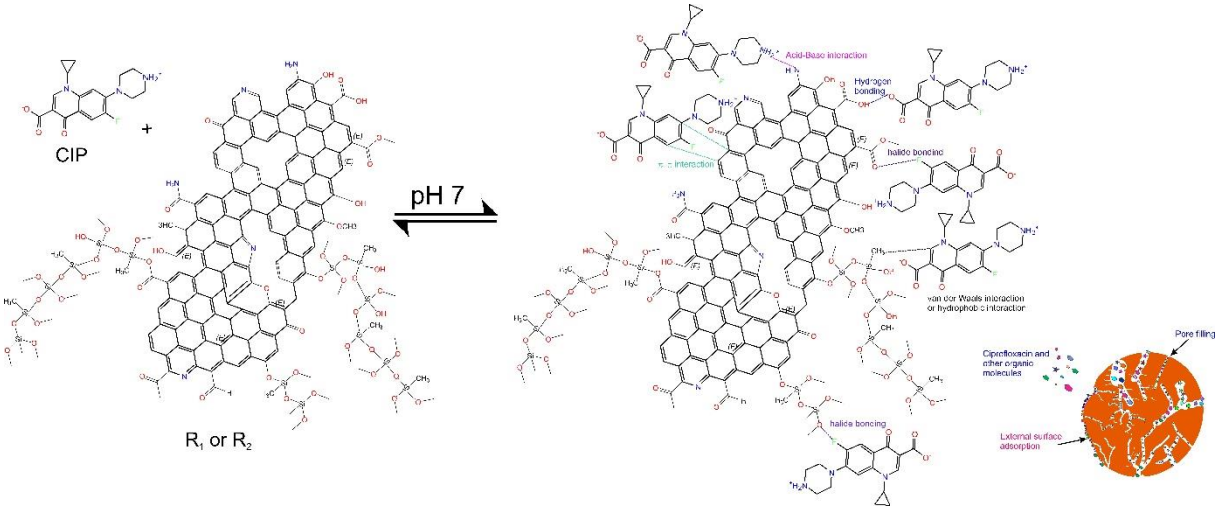
CIP
+
pH 7
R1 or R2
Acid-Base interaction
Hydrogen bonding
π - π interaction
halide bonding
van der Waals interaction or hydrophobic interaction
halide bonding
Pore filling
Ciprofloxacin and other organic molecules
External surface adsorption

985